



# A phase-field formulation for cohesive fracture based on the Park–Paulino–Roesler (PPR) cohesive fracture model

Rogelio A. Muñetón-López, Oliver Giraldo-Londoño \*

Department of Civil and Environmental Engineering, University of Missouri, Columbia, MO 65211, USA

## ARTICLE INFO

### Keywords:

Cohesive zone models  
Traction–separation relationship  
Phase-field  
FEM

## ABSTRACT

Unlike most cohesive zone models (CZMs), the Park–Paulino–Roesler (PPR) cohesive fracture model has the inherent ability to control the softening shape of the traction–separation relationships, which makes it suitable to model fracture for a wide variety of materials. Like other CZMs, the PPR model is well-suited for problems where the crack path is known a priori but its implementation may become complex in situations where the crack path is not known beforehand. To overcome this limitation, we recast the PPR model within the framework of the phase field method, which enables the modeling of crack propagation problems with complex crack topologies using a straightforward multi-field finite element implementation. We use constitutive functions (i.e., crack geometric function and degradation function) consistent with the PPR model for the case of mode-I fracture, such that equivalent traction–separation relationships from the phase-field model approximate those from the original PPR model. Our choice of geometric and degradation functions is based upon those proposed by Wu (2017). We present several numerical examples to demonstrate the ability of the model to capture fracture of problems with different materials, geometries, and boundary conditions. Also, we show that the results from our model converge to those obtained with the original PPR model for problems where the crack path is known a priori. Being crucial in engineering design, we finally show that the model can capture size and boundary effects with satisfactory accuracy.

## 1. Introduction

The phase-field method has gained popularity in recent years due to its ability to model crack propagation problems with complex crack topologies using a relatively straightforward multi-field finite element implementation. The phase-field method regularizes a sharp crack surface using a scalar auxiliary field — the phase field, which interpolates between the unbroken and the broken state of the material. Although effective, the phase-field method has mainly been developed to model fracture of brittle materials for which Griffith's description of fracture applies (Griffith, 1921). However, most materials are not perfectly brittle and display some ductility after reaching their ultimate strength. These materials, typically referred to as quasi-brittle materials, cannot be modeled using Griffith's theory, and instead require theories based on nonlinear fracture mechanics (Bažant and Oh, 1983).

One of the most popular numerical techniques used to simulate fracture of quasi-brittle materials is based on the cohesive zone concept (Barenblatt, 1959; Dugdale, 1960). According to this concept, as a fracture propagates, cohesive surfaces with prescribed traction–separation laws are inserted in front of the crack tip to model the breakage of bonds as the surfaces separate. During separation, the cohesive tractions initially increase until reaching a maximum value (i.e., the cohesive strength) and then decrease to zero, leading to macroscopic crack formation. Classical cohesive zone models (CZMs) found in the literature have either a linear

\* Corresponding author.

E-mail address: [ogiraldo@missouri.edu](mailto:ogiraldo@missouri.edu) (O. Giraldo-Londoño).

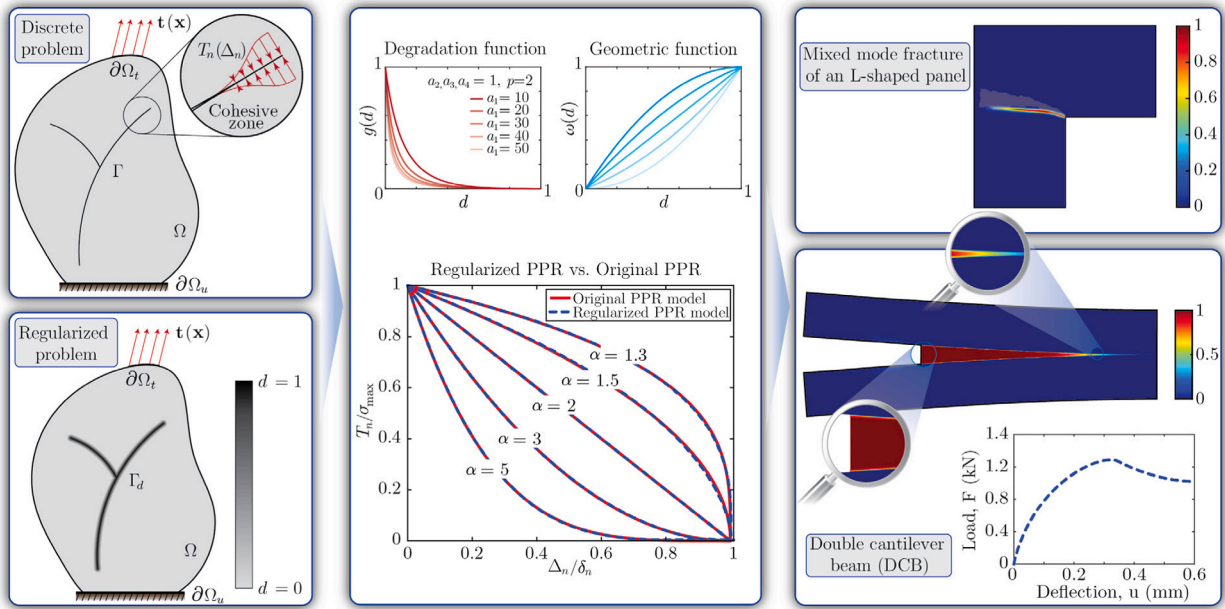


**Fig. 1.** Overview of the proposed *regularized PPR* model for cohesive fracture: On the left, the two figures depict schematics of a discrete crack (top) featuring a cohesive zone model and a regularized crack (bottom) where the phase-field variable is introduced to regularize the crack surface. In the middle section, a rational degradation function and a quadratic geometric function (middle top) are employed to derive traction-separation relationships consistent with the original PPR model (middle bottom). On the right, the two figures display illustrative numerical results, which are explained in detail later, showcasing the ability of our model to capture various fracture phenomena.

or a convex (e.g., exponential) softening response (Needleman, 1987; Freed and Banks-Sills, 2008; Needleman, 1990a,b; Xu and Needleman, 1993), whose shape cannot be modified. Several studies have shown that the softening shape of a CZM can affect the simulated fracture behavior of a given specimen (Volokh, 2004; Alfano, 2006; Song et al., 2008), which highlights the need for a CZM capable of controlling the shape of the softening response.

The Park–Paulino–Roesler (PPR) CZM (Park et al., 2009) is a potential-based model which can control the softening shape of the traction–separation response. The intrinsic version of the PPR model has primarily been used to simulate delamination problems (Park et al., 2009; Spring et al., 2016; Giraldo-Londoño et al., 2018, 2019), for which the crack path is known a priori. The extrinsic version of the PPR model has been used for dynamic fracture simulations (e.g., see Leon et al. (2014), Spring et al. (2014)), which requires adaptive insertion of cohesive elements as the crack propagates. Although conceptually simple, adaptive insertion of cohesive elements requires on the fly modifications of the mesh topology, which are nontrivial. Moreover, crack propagation is restricted to propagate along element facets, producing mesh-dependent crack paths (e.g., see Leon et al. (2014)).

To circumvent the issues raised above, the present work aims to recast the PPR model within the framework of the phase-field method. This work is based upon the work by Wu (2017, 2018) on phase-field regularized cohesive fracture. Here, we use two constitutive functions, the crack geometric function and the degradation function, as introduced in Wu (2017), to model the material behavior during fracture. The parameters used to define both functions are specifically tuned to approximate the mode-I behavior of the extrinsic PPR model for an arbitrary shape parameter. Unlike existing phase-field models, this formulation, which we call the *regularized PPR model*, can reproduce traction–separation curves with concave, convex, or linear softening responses as demonstrated in Fig. 1.

The remainder of this paper is organized as follows. In Section 2, we summarize relevant studies in the literature as it pertains to phase-field models for brittle and cohesive fracture. Next, in Section 3, we briefly discuss the fundamentals of the phase-field method for quasi-brittle fracture, followed by a discussion of the regularized PPR model in Section 4. We discuss the finite element (FE) formulation in Section 5 and present several numerical examples in Section 6 to showcase the effectiveness of the proposed approach. We finalize the paper with some concluding remarks and future research directions. Afterward, we provide an Appendix that contains the nomenclature employed in our work.

## 2. Background

Many engineering materials and structures fail due to fracture propagation. For instance, concrete structures typically fail when tensile stresses break the bond between matrix and aggregates or when microcracks and pores inside the matrix enlarge due to loading. Understanding the mechanics of damage and failure of engineering materials is essential for assessing structural integrity and potentially preventing catastrophic collapse of engineering structures. Two main approaches exist for the modeling of crack

propagation in engineering materials: discrete crack approaches and smeared crack approaches.<sup>1</sup> In discrete crack approaches, discontinuities are modeled explicitly as discrete entities while in smeared crack approaches discontinuities are distributed over a finite width (i.e., cracked surfaces are smeared out over the domain). The cohesive zone model approach (Park and Paulino, 2011) is an example of a discrete crack approach while the phase-field method (Bourdin et al., 2000; Miehe et al., 2010a,b) is an example of a smeared crack approach.

For problems in which the location of discontinuities is known (e.g., across grain boundaries or for delamination problems), discrete approaches such as the CZM are desirable, because one can easily create a conforming mesh in which the discontinuities are modeled explicitly. When the location of discontinuities is unknown (e.g., as it is the case for arbitrary crack propagation in most engineering structures), the use of CZMs typically requires cohesive elements to be inserted on the fly as the crack evolves, which requires modifications of the mesh topology each time a cohesive element is inserted. In such cases, smeared crack approaches such as the phase-field method are an attractive alternative.

Early developments of the phase-field method are built upon Griffith's description of brittle fracture (Griffith, 1921). Griffith's theory cannot determine curvilinear crack paths, or crack kinking and branching and cannot predict crack initiation. These limitations were later overcome by the variational formulation proposed by Francfort and Marigo (1998). In their work, Griffith's theory of fracture is rewritten as a minimization problem seeking to find the configuration that minimizes the total energy of the cracking solid, yielding a formulation that can capture crack initiation and propagation in a unified way. A regularized version of their variational formulation was later developed by Bourdin et al. (2000) and Bourdin et al. (2008), which led to the development of the phase-field method.

Within a unified framework, the phase-field formulation by Bourdin et al. (2000) can model crack nucleation, propagation, branching, and coalescence for either 2D or 3D problems, but it predicts identical fracture in tension or compression, producing non-physical results for compression or shear dominated problems. A common strategy to alleviate this limitation is to decompose the strain energy density function into a tension-dominated and a compression-dominated part and allow fracture to occur only under tension. One of such models is that by Amor et al. (2009), in which the strain energy density is decomposed into a volumetric and a deviatoric component by decomposing the stiffness tensor. The volumetric component is responsible for the isotropic response of the material and prevents cracking in compression, while the deviatoric component accounts for the anisotropic behavior of the material and allows for crack propagation in tension. Another model is that by Miehe et al. (2010a,b), in which the strain energy density is split into a positive and a negative component via spectral decomposition of the strain tensor. Another popular alternative is that by Wu and Nguyen (2018), in which they considered a positive and a negative decomposition of the effective stress, similar to the strain tensor decomposition, to prevent cracking under compression.

From the phase-field models discussed above, that by Miehe et al. (2010a,b) was derived within the framework of thermodynamics. In their work, they discussed two numerical implementations known today as the monolithic and staggered approaches to phase-field modeling, which spurred a myriad of new studies in the phase-field method. Later, the work by Miehe et al. was extended to dynamic fracture (Hofacker and Miehe, 2013; Borden et al., 2014), and more recently, a simplified version of the model by Miehe et al. (2010a,b) was implemented using user-defined subroutines in Abaqus (Msekh et al., 2015). For the sake of brevity, interested readers are referred to Ambati et al. (2015) for a detailed review of phase-field models for brittle fracture.

Most studies on the phase-field method are focused on brittle fracture, while just a few of them have been focused on quasi-brittle fracture. Bourdin et al. (2008) were the first to extend the variational formulation for brittle fracture to cohesive fracture which was later recast by Verhoosel and De Borst (2013) in the context of the phase-field method by introducing a second auxiliary field that captures the displacement jump across the fracturing surfaces. The approach by Verhoosel and De Borst (2013) is limited to problems for which the crack path is known a priori. Moreover, the introduction of the second auxiliary field induces stress oscillations which can only be avoided if different interpolation orders are used for the different auxiliary fields (see Vignollet et al. (2014), May et al. (2015)). Later, Conti et al. (2016) and Freddi and Iurlano (2017) introduced a new phase-field model for cohesive fracture. Their cohesive zone formulation was derived by analyzing the response of a bar subjected to traction and using the solution to reconstruct the traction–separation response of an exponential CZM via a backtracking process. More recently, Wu and Nguyen (2018) introduced a length-scale insensitive phase-field model for brittle fracture based on a CZM with linear softening. This was accomplished by using a rational degradation function whose coefficients are obtained to replicate the linear softening response on a 1D bar subjected to traction. The same rational function was adopted by Wu (2017, 2018) to reproduce both linear and exponential cohesive softening responses. In our work, we build upon the work by Wu and co-workers and incorporate an additional term into the rational degradation function, enabling us to capture convex, linear, and concave softening responses.

### 3. Fundamentals of phase-field methods for quasi-brittle fracture

This section introduces the essential theoretical aspects of phase-field formulations for quasi-brittle fracture, laying the groundwork for the derivation of our phase-field formulation in the following section. Consider a domain  $\Omega$  with a discrete crack,  $\Gamma$ , as shown in Fig. 2a. The domain is loaded with surface tractions  $\mathbf{t}$  prescribed at the portion of the boundary,  $\partial\Omega_t$ , and supported on the portion of the boundary,  $\partial\Omega_u$ . When considering the phase-field method, the discrete crack,  $\Gamma$ , is approximated by its smeared counterpart,  $\Gamma_d$ , as shown in Fig. 2b, by introducing a scalar field,  $d$  — the phase-field. This new field varies between 0 and 1 to represent the unbroken and broken state of the material, respectively.

<sup>1</sup> In addition to discrete and smeared crack approaches, there are other methods that have proven effective for simulating crack propagation in engineering and material science applications such as the Material Point Method (MPM), Peridynamics, and the Extended Finite Element Method (XFEM); however, those methods are out of the scope of the present work.

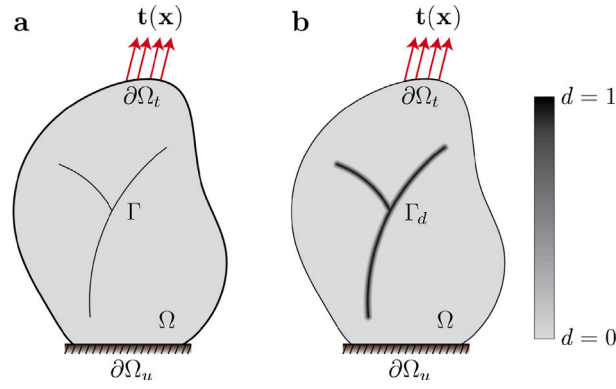


Fig. 2. Schematic representation of a solid domain  $\Omega$  with (a) a discrete crack  $\Gamma$  and (b) a smeared crack  $\Gamma_d$ .

The total potential energy,  $\Pi$ , of the discretely cracked body in Fig. 2a is given by

$$\Pi = U(\boldsymbol{\varepsilon}, \Gamma) - W_{\text{ext}}(\mathbf{u}), \tag{1}$$

where

$$U(\boldsymbol{\varepsilon}, \Gamma) = \int_{\Omega \setminus \Gamma} \psi_0(\boldsymbol{\varepsilon}) dV + \int_{\Gamma} \phi_n dS \tag{2}$$

is the stored energy of the cracking body, which consists of the bulk and fracture contributions, respectively;  $\psi_0(\boldsymbol{\varepsilon})$  is the strain energy density of the bulk material, where  $\boldsymbol{\varepsilon}(\mathbf{u}) := \frac{1}{2}(\nabla \mathbf{u} + \nabla \mathbf{u}^T)$  is the infinitesimal strain tensor, and  $\phi_n$  is the mode I fracture energy. Moreover,

$$W_{\text{ext}}(\mathbf{u}) = \int_{\Omega} \mathbf{f} \cdot \mathbf{u} dV + \int_{\partial\Omega_t} \mathbf{t} \cdot \mathbf{u} dS \tag{3}$$

is the external potential energy of the system, where  $\mathbf{f}$  is the distributed body force and  $\mathbf{u}$  is the displacement field. Following the regularized approach by Bourdin et al. (2000), the total potential energy (1) is approximated as

$$\tilde{\Pi} = \tilde{U}(\boldsymbol{\varepsilon}, d) - W_{\text{ext}}(\mathbf{u}), \tag{4}$$

where

$$\tilde{U}(\boldsymbol{\varepsilon}, d) = \int_{\Omega} \psi_{\text{bulk}}(\boldsymbol{\varepsilon}, d) dV + \int_{\Omega} \phi_n \gamma(d, \nabla d) dV \tag{5}$$

is the regularized stored energy, in which  $\gamma(d, \nabla d)$  is the crack surface density function and  $\psi_{\text{bulk}}(\boldsymbol{\varepsilon}, d)$  is the degrading strain energy density in the bulk given by

$$\psi_{\text{bulk}}(\boldsymbol{\varepsilon}, d) = g(d)\psi_0(\boldsymbol{\varepsilon}), \tag{6}$$

where  $g(d) \in [0, 1]$  is a stiffness degradation function which accounts for the degradation of the initial strain energy  $\psi_0(\boldsymbol{\varepsilon})$  as the phase-field values increase.

### 3.1. Crack surface density function and geometric function

Following the work by Miehe et al. (2010a,b), the crack surface density function,  $\gamma(d, \nabla d)$ , is used to regularize the sharp crack topology. In particular,  $\gamma(d, \nabla d)$  is used to approximate the Dirac-delta function,  $\delta_s$ , such that the regularized crack surface,

$$A_d = |\Gamma_d|,$$

is computed as

$$A_d(d) = \int_{\Omega} \gamma(d, \nabla d) dV \approx \int_{\Omega} \delta_s dV = \int_{\Gamma} dS = A_s,$$

where  $A_s = |\Gamma|$  is the surface area of the sharp crack. The crack surface density function is typically expressed in terms of the crack phase field and its gradient, as follows (Wu, 2017):

$$\gamma(d, \nabla d) := \frac{1}{c_0} \left( \frac{1}{l_0} \omega(d) + l_0 |\nabla d|^2 \right), \tag{7}$$

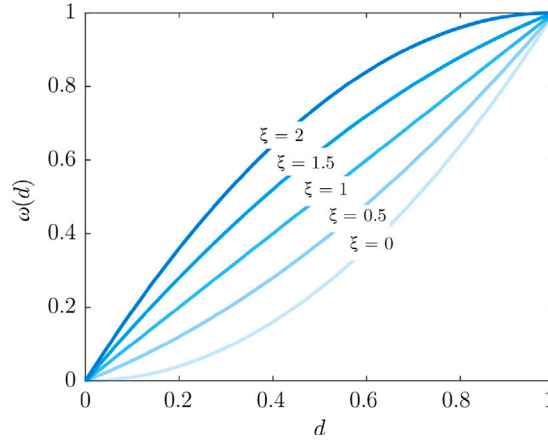


Fig. 3. Geometric function,  $\omega(d)$ , from Eq. (8), for various values of  $\xi$ .

where

$$c_0 = 4 \int_0^1 \sqrt{\omega(d)} dd$$

is a scaling parameter,  $\omega(d)$  is a geometric function that characterizes the continuous evolution of the phase field, and  $l_0$  is a length-scale parameter that controls the extent of the crack surface regularization. The geometric function must satisfy  $\omega(0) = 0$  so that the regularized crack surface,  $A_d$ , is zero for the unbroken state, and  $\omega(1) = 1$  to represent the sharp crack surface,  $A_s$ , for the fully broken state (Wu, 2017; Miehe et al., 2010b). A typical choice of geometric function used in phase-field models for brittle fracture is  $\omega(d) = d^2$  (Miehe et al., 2010a,b). This function makes the phase-field problem linear, which is computationally efficient, and the bounds  $0 \leq d \leq 1$  are inherently satisfied. Another typical choice in phase-field models for brittle fracture is the linear geometric function  $\omega(d) = d$  introduced by Pham et al. (2011). This function restores the elastic state of the material before damage nucleation. In the context of quasi-brittle fracture, Wu (2017) adopted the following geometric function, which is a generalization of the two geometric functions discussed above:

$$\omega(d) = \xi d + (1 - \xi) d^2 \quad \forall d \in [0, 1]. \quad (8)$$

Here,  $\xi \in [0, 2]$  is a scalar parameter to guarantee that  $\omega(d)$  is bounded between 0 and 1. Fig. 3 illustrates the geometric function for different values of  $\xi$ . In our work, we consider  $\omega(d) = 2d - d^2$  (i.e.,  $\xi = 2$ ) as this option is compatible with phase-field formulations for cohesive fracture, and more importantly, it guarantees the  $\Gamma$ -convergence of the phase-field model for  $l_0 \rightarrow 0$  (Wu, 2017).<sup>2</sup>

### 3.2. Degradation function

The degrading strain energy density in the bulk from Eq. (6) is affected by a degradation function  $g(d)$  that determines the way the stored energy functional responds to changes in the crack phase-field. The degradation function must decrease monotonically for  $d \in [0, 1]$  (i.e.,  $g'(d) < 0 \quad \forall d \in [0, 1]$ ), and must satisfy  $g(0) = 1$  for the unbroken state and  $g(1) = 0$  for the fully broken state. Moreover,  $g(d)$  must satisfy  $g'(1) = 0$  to ensure that the energetic fracture force converges to a finite value when the material is fully broken (Miehe et al., 2010b).

Different degradation functions have been proposed in the literature, with the quadratic polynomial,  $g(d) = (1 - d)^2$ , being the most popular one in standard phase-field models for brittle fracture (Bourdin et al., 2000; Miehe et al., 2010a,b). For quasi-brittle fracture, Wu (2017) proposed a generic rational degradation function of the form:

$$g(d) = \frac{(1 - d)^p}{(1 - d)^p + Q(d)}, \quad \text{with } p > 0, \quad (9)$$

where

$$Q(d) = a_1 d \cdot P(d), \quad \text{with } P(d) = 1 + a_2 d + a_3 d^2. \quad (10)$$

<sup>2</sup> Among all the geometric functions discussed above, the typical geometric function implemented in brittle fracture, i.e.,  $\omega(d) = d^2$ , is the only one that yields  $d = 0$  in the absence of mechanical strains. Conversely, a geometric function such as that given by (8) yields  $d \neq 0$  in the absence of mechanical strains so that special strategies are needed to ensure that  $d$  remains bounded between 0 and 1 during the entire loading history (Wu et al., 2019; Zhang et al., 2018). Additional details regarding this issue will be provided later.

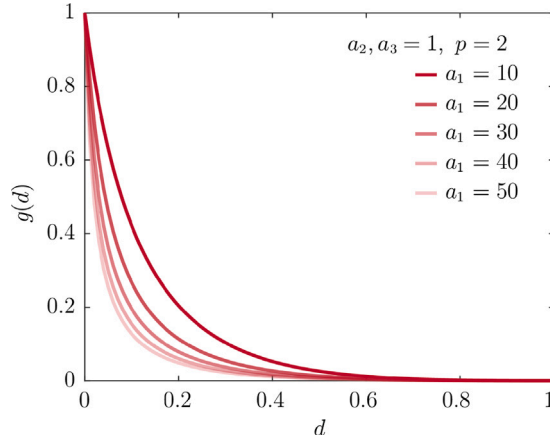


Fig. 4. Rational degradation function,  $g(d)$ , from (9), for various values of  $a_1$ .

The coefficients  $a_1, a_2, a_3$ , and  $p$  are all parameters to be calibrated. Fig. 4 shows different curves for  $g(d)$  by fixing  $a_2, a_3$ , and  $p$  and varying  $a_1$ . As we will discuss later, in this work we adopt the rational degradation function (9) but use a higher-degree polynomial  $P(d)$  to enable the phase-field model to capture cohesive zone models of arbitrary softening shape.

### 3.3. Governing balance equations

Following the procedure outlined by Miehe et al. (2010b), the total potential energy (4) can be used to obtain the corresponding balance equations for the uncoupled displacement and phase field problems (i.e., adopting a staggered approach). The displacement  $\mathbf{u}$  and phase-field  $d$  are determined by solving the minimization problem

$$(\mathbf{u}(\mathbf{x}), d(\mathbf{x})) = \text{Arg}\{\min \tilde{\Pi}(\mathbf{u}, d)\} \text{ s.t. } d \geq 0, d \in [0, 1]. \tag{11}$$

By taking the first variation of the energy functional (4) with respect to  $\mathbf{u}$  and applying the divergence theorem (Wu et al., 2019), we obtain the following governing equations in strong form for the displacement field:

$$\begin{aligned} \delta \tilde{\Pi}^{\mathbf{u}} \geq 0 \rightarrow \nabla \cdot \boldsymbol{\sigma} + \mathbf{f} &= \mathbf{0} \text{ in } \Omega, \\ \boldsymbol{\sigma} \cdot \mathbf{n} &= \mathbf{t} \text{ on } \partial\Omega_t. \end{aligned} \tag{12}$$

Similarly, the first variation of (4) with respect to  $d$  leads to

$$\delta \tilde{\Pi}^d \geq 0 \rightarrow Y - \phi_n \frac{1}{c_0} \left[ \frac{1}{l_0} \omega'(d) - 2l_0 \Delta d \right] \leq 0. \tag{13}$$

The stress tensor,  $\boldsymbol{\sigma}$ , in (12) and the thermodynamic driving force,  $Y$ , in (13) are respectively given by:

$$\boldsymbol{\sigma} = \frac{\partial \Psi_{bulk}}{\partial \boldsymbol{\varepsilon}} = g(d) \frac{\partial \Psi_0}{\partial \boldsymbol{\varepsilon}} = g(d) \bar{\boldsymbol{\sigma}} \text{ and} \tag{14}$$

$$Y = -\frac{\partial \Psi_{bulk}}{\partial d} = -\frac{\partial \Psi_{bulk}}{\partial g} \frac{\partial g}{\partial d} = -g'(d) \mathcal{Y}, \text{ with } \mathcal{Y} := \frac{\partial \Psi_{bulk}}{\partial g}, \tag{15}$$

where  $\bar{\boldsymbol{\sigma}}$  is the effective stress tensor, and  $\mathcal{Y}$  is the effective crack driving force. The effective stress tensor is obtained as

$$\bar{\boldsymbol{\sigma}} = \frac{\partial \Psi_0}{\partial \boldsymbol{\varepsilon}} = \mathbb{E}_0 : \boldsymbol{\varepsilon}, \tag{16}$$

where  $\mathbb{E}_0$  is the elastic stiffness tensor. The non-negative thermodynamic force,  $Y$ , in (15) drives the evolution of the phase field and is written in terms of the effective crack driving force  $\mathcal{Y}$  that represents the elastic strain energy of the undamaged material (Wu, 2017). For an isotropic elastic body, the effective crack driving force,  $\mathcal{Y}$ , is equal to the elastic strain energy,  $\Psi_0(\boldsymbol{\varepsilon})$ . That is,

$$\mathcal{Y} = \Psi_0(\boldsymbol{\varepsilon}) = \frac{1}{2} \boldsymbol{\varepsilon} : \mathbb{E}_0 : \boldsymbol{\varepsilon}. \tag{17}$$

Cracks are typically initiated by the local accumulation of tensile stresses, which can occur due to material defects or geometric irregularities. However, from Eq. (17), we cannot differentiate between tension and compression, so a phase-field model with this formulation, although it is variationally consistent, may predict cracks that are not realistic. In order to prevent cracks under compression, different alternatives for the elastic strain energy have been applied in phase-field models. One of the most widely used is the anisotropic model of Miehe et al. (2010b) which consists of splitting the strain tensor into a positive and a negative component to differentiate between tension and compression. This splitting allows the degradation function to affect only the damaged part of

the material corresponding to the tension component of the elastic energy, thus avoiding the creation of cracks under compression. However, this tension/compression split makes the displacement problem nonlinear increasing the computational time considerably.

Other alternatives to avoid cracks under compression are the so-called hybrid models in which a different effective crack driving force,  $\mathcal{Y}$ , is used for the evolution law of the crack phase-field (15). Hybrid models are computationally more efficient than strain energy decomposition approaches, such as that proposed by Mische et al. (2010b), because the displacement problem becomes linear in the former. Ambati et al. (2015) compared the hybrid approach with the tension–compression split formulation by Mische et al. (2010b) for brittle problems and found the results to be very similar with savings in the computational cost of about one order of magnitude. Although hybrid formulations are no longer variationally consistent, it has been proven that the second law of thermodynamics<sup>3</sup> is not violated (Wu, 2018). In this work, we adopt a hybrid approach and consider the following modified effective crack driving force (Wu, 2017):

$$\bar{\mathcal{Y}} = \frac{1}{2E_0} \bar{\sigma}_{\text{eq}}^2 \quad \text{with} \quad \bar{\sigma}_{\text{eq}} = \frac{1}{1 + \beta_c} \left( \beta_c \langle \bar{\sigma}_1 \rangle + \sqrt{3\bar{J}_2} \right), \quad (18)$$

where  $E_0$  is the Young's modulus of the material;  $\beta_c = f_c/f_t - 1$ , where  $f_c$  and  $f_t$  are the uniaxial compressive and tensile strengths of the material, respectively;<sup>4</sup>  $\langle \bar{\sigma}_1 \rangle = \max(\bar{\sigma}_1, 0)$ , where  $\bar{\sigma}_1$  is the maximum principal value of the effective stress tensor; and  $\bar{J}_2$  is the second invariant of the deviatoric (effective) stress tensor, which can be obtained in terms of the principal stresses as

$$\bar{J}_2 = \frac{1}{6} \left[ (\bar{\sigma}_1 - \bar{\sigma}_2)^2 + (\bar{\sigma}_2 - \bar{\sigma}_3)^2 + (\bar{\sigma}_3 - \bar{\sigma}_1)^2 \right]. \quad (19)$$

Following Mische et al. (2010b), we consider the so-called history field  $\mathcal{H}$  to enforce irreversibility of the phase-field. Replacing the thermodynamic driving force  $Y$  by  $-g'(d)\mathcal{H}$  in the balance equation (13) yields:<sup>5</sup>

$$g'(d)\mathcal{H} + \phi_n \frac{1}{c_0} \left[ \frac{1}{l_0} \omega'(d) - 2l_0 \Delta d \right] = 0, \quad \text{with} \quad \mathcal{H} = \max_{\tau \in [0, t]} \bar{\mathcal{Y}}(\mathbf{x}, \tau). \quad (20)$$

As discussed previously, unlike traditional phase-field approaches that use a geometric function of the form  $\omega(d) = d^2$ , those using a geometric function such as that in (8) require damage boundedness  $d \in [0, 1]$  to be enforced. Zhang et al. (2018) proposed a simple strategy that consists of modifying the history field,  $\mathcal{H}$ , in (20) as follows:

$$\mathcal{H} = \max_{\tau \in [0, t]} [\bar{\mathcal{Y}}(\mathbf{x}, \tau), \bar{\psi}], \quad (21)$$

where  $\bar{\psi} = \frac{\sigma_{\text{max}}^2}{2E_0}$  represents the critical energy required to obtain a zero phase-field value. In this study, we adopt the strategy by Zhang et al. (2018) due to its simplicity and efficacy.

### 3.4. Equivalent cohesive zone model

In this work, we use the equivalent traction–separation law presented by Wu (2017) from which expressions for the calibration parameters  $a_1, a_2, a_3$ , from (10), can be obtained. Wu (2017) considered a 1D bar with  $x \in [-L, L]$ , subjected to an increasing displacement  $u^*$  at both ends. Assuming symmetry and homogeneity, it can be anticipated that, as damage initiates and evolves, the maximum value for the phase-field,  $d^*$ , will be located at  $x = 0$ . Using the geometric function (8) with  $\xi = 2$  and the degradation function (9)–(10), the balance equation (12) and the damage evolution equation (13) can be solved for the idealized 1D bar. The solution results in expressions for the apparent displacement jump,  $\Delta_n$ , and traction,  $T_n$ , as a function of the maximum value of the damage parameter,  $d^*$ , along the bar length at the symmetric point  $x = 0$ . The stress and apparent displacement jump define an apparent traction–separation response or an equivalent cohesive zone model given by

$$T_n(d^*) = \sigma_{\text{max}} \sqrt{\frac{(2 - d^*)(1 - d^*)^p}{2P(d^*)}} \quad \text{and} \quad (22)$$

$$\Delta_n(d^*) = \frac{4\sqrt{2}\phi_n}{\pi\sigma_{\text{max}}} \int_0^{d^*} \left[ \frac{P(d^*)}{(1 - d^*)^p} \frac{2 - d}{2 - d^*} - \frac{P(d)}{(1 - d)^p} \right]^{-1/2} \frac{\sqrt{d}P(d)}{(1 - d)^p} dd. \quad (23)$$

Using Eqs. (22)–(23), expressions for the calibration parameters  $a_1, a_2, a_3$  from (10) are obtained using the cohesive strength,  $\sigma_{\text{max}}$ , the initial slope,  $k_0$ , and the final crack opening,  $\delta_n$ , as follows:

$$\sigma_{\text{max}} := \lim_{d^* \rightarrow 0} T_n(d^*) \Rightarrow a_1 = \frac{4}{\pi l_0} \cdot \frac{E_0 \phi_n}{\sigma_{\text{max}}^2}, \quad (24)$$

<sup>3</sup> The second law of thermodynamics implies that the crack growth process is inherently dissipative and irreversible, leading to a loss of mechanical energy and an increase in the internal energy of the material.

<sup>4</sup> The value of  $\beta_c$  is typically determined empirically or experimentally and can vary depending on the specific material being studied. The relation  $f_c/f_t$  is usually taken to be equal to 10 for normal concrete. The maximum normal stress criterion, or Rankine criterion, which can well predict the fracture of brittle materials is recovered for  $\beta_c \rightarrow \infty$ .

<sup>5</sup> Note that the history field,  $\mathcal{H}$ , in (20) is defined in terms of the modified effective crack driving force (18) instead of the maximum positive strain energy density employed by Mische et al. (2010b). This choice is motivated by previous work by Wu (2017), who showed that (18) is effective to model quasi-brittle fracture problems.

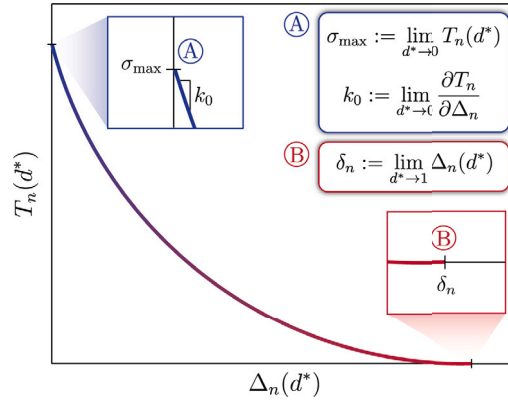


Fig. 5. Arbitrary apparent traction–separation curve obtained with the equivalent cohesive zone model (22)–(23). At the onset of crack nucleation (point A), when  $d^* = 0$ , we obtain  $\sigma_{\max}$  and  $k_0$  using Eqs. (24)–(25). Also, at the fully broken state (point B), when  $d^* = 1$ , we obtain  $\delta_n$  using Eq. (26).

$$k_0 := \lim_{d^* \rightarrow 0} \frac{\partial T_n}{\partial \Delta_n} \Rightarrow a_2 = 2 \left( -2k_0 \frac{\phi_n}{\sigma_{\max}^2} \right)^{2/3} - \left( p + \frac{1}{2} \right), \text{ and} \tag{25}$$

$$\delta_n := \lim_{d^* \rightarrow 1} \Delta_n(d^*) \Rightarrow a_3 = \begin{cases} 0, & p > 2 \\ \frac{1}{a_2} \left[ \frac{1}{8} \left( \frac{\delta_n \sigma_{\max}}{\phi_n} \right)^2 - (1 + a_2) \right], & p = 2. \end{cases} \tag{26}$$

To facilitate the interpretation of Eqs. (24)–(26), Fig. 5 provides graphical definitions of the cohesive strength,  $\sigma_{\max}$ , initial slope,  $k_0$ , and final crack opening,  $\delta_n$ , for an arbitrary traction–separation curve. As shown by the figure,  $\sigma_{\max}$  and  $k_0$  correspond to the cohesive strength and initial slope of the traction–separation curves, which can be evaluated from (22) at the onset of fracture initiation (i.e., when  $d^* \rightarrow 0$ ). Moreover,  $\delta_n$  corresponds to the crack opening at which the cohesive traction becomes zero and can be obtained from (23) when  $d^* \rightarrow 1$ . For the sake of brevity, interested readers are referred to Wu (2017) for details on the derivations leading to Eqs. (22)–(26).

Parameters  $a_1, a_2, a_3$  in Eqs. (24)–(26) can be calibrated as follows. From Eq. (24) it can be noticed that parameter  $a_1$  only depends on material properties and the internal length-scale parameter,  $l_0$ .<sup>6</sup> In contrast, parameters  $a_2$ , and  $a_3$  require the choice of a softening law (e.g. linear, exponential, hyperbolic, Cornelissen) from which the initial slope,  $k_0$  (25), and the final crack opening,  $\delta_n$  (26), can be obtained (Wu, 2017).

#### 4. Regularized PPR model

This section discusses the proposed PPR-based phase-field model, herein referred to as the *regularized PPR model*. We begin with a short description of the extrinsic PPR cohesive fracture model (Park et al., 2009) followed by the derivation of the regularized PPR model.

##### 4.1. Extrinsic PPR cohesive fracture model

The Park–Paulino–Roesler (PPR) cohesive zone model (Park et al., 2009) is a mixed-mode potential-based model which considers different fracture energies in modes I and II simultaneously. In its most general form, the extrinsic PPR potential is given as

$$\Psi(\Delta_n, \Delta_t) = \min(\phi_n, \phi_t) + \left[ \Gamma_n \left( 1 - \frac{\Delta_n}{\delta_n} \right)^\alpha + \langle \phi_n - \phi_t \rangle \right] \times \left[ \Gamma_t \left( 1 - \frac{|\Delta_t|}{\delta_t} \right)^\beta + \langle \phi_n - \phi_t \rangle \right], \tag{27}$$

where  $\phi_n$  and  $\phi_t$  are the mode-I and mode-II fracture energies, respectively,  $\Gamma_n = -\phi_n$  and  $\Gamma_t = 1$  (when  $\phi_n = \phi_t$ ) are energy constants,  $\Delta_n$  and  $\Delta_t$  are the normal and tangential crack opening displacements,  $\delta_n$  and  $\delta_t$  are the normal and tangential final crack opening widths, and  $\alpha > 1$  and  $\beta > 1$  are non-dimensional shape parameters controlling the shape of the normal and tangential softening responses, respectively.

<sup>6</sup> It is suggested that the length scale parameter be a numerical parameter rather than a material property, which typically results in values that are not small enough to resolve the regularized crack surface (Wu, 2018). Additionally, taking  $l_0$  as a numerical parameter allows for the definition of a general traction–separation law within the framework of Barenblatt’s CZM (Barenblatt, 1959) since the failure strength and general softening law (Eqs. (22)–(23)) will be independent of it. In this sense, global responses insensitive to  $l_0$  can be guaranteed (Wu, 2018).

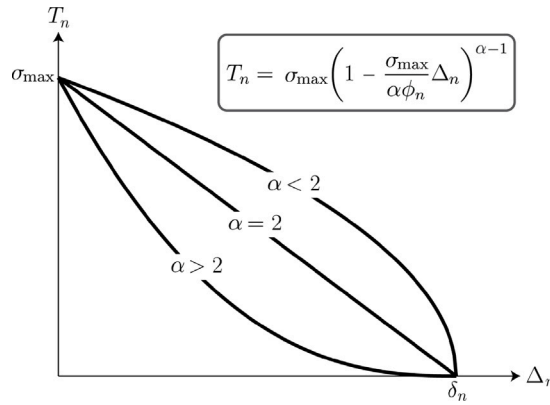


Fig. 6. Range of traction–separation relationships achievable with the mode-I PPR cohesive fracture model. Note that the PPR model predicts convex softening responses when  $\alpha < 2$ , linear softening responses when  $\alpha = 2$ , and concave softening responses when  $\alpha > 2$ .

To derive the regularized PPR model, this study only considers the component of the PPR potential corresponding to mode-I tractions.<sup>7</sup> After replacing  $\phi_n = \phi_t$  and  $\Delta_t = 0$  into Eq. (27), the extrinsic PPR potential simplifies to

$$\Psi(\Delta_n) = \phi_n \left[ 1 - \left( 1 - \frac{\Delta_n}{\delta_n} \right)^\alpha \right]. \tag{28}$$

Knowing that the final crack opening width in mode-I is equal to  $\delta_n = \alpha \phi_n / \sigma_{\max}$  (Park et al., 2009), the mode-I cohesive traction,  $T_n$ , obtained from the PPR potential (28) is given by:

$$T_n = \frac{\partial \Psi_n}{\partial \Delta_n} = \sigma_{\max} \left( 1 - \frac{\sigma_{\max}}{\alpha \phi_n} \Delta_n \right)^{\alpha-1}. \tag{29}$$

As shown in Fig. 6, the softening response of the extrinsic PPR cohesive fracture model is convex when  $\alpha > 2$ , concave when  $\alpha < 2$ , and linear when  $\alpha = 2$ .

The mode-I PPR potential (28) is a continuous polynomial that provides a finite final crack opening width. However, the potential may predict non-zero tractions for physical separations greater than the final crack opening width. Therefore, the potential should be defined in a valid softening domain. In this case, for the mode-I cohesive traction (29) the domain is limited by the normal final crack opening width  $\delta_n$ , which means that if  $\Delta_n > \delta_n$ , the normal traction,  $T_n$ , is set to zero (Park et al., 2009).

#### 4.2. Regularized PPR model

The extrinsic PPR cohesive fracture model (29), hereinafter referred to as the original PPR model, can describe convex, concave, or linear softening responses depending on the value of the shape parameter  $\alpha$  (see Fig. 6). To drive a phase-field model capable of recovering these types of cohesive softening responses, we rely on the general form of the apparent traction–separation relationship given in Eqs. (22)–(23). Note that the apparent traction–separation relationship depends on parameter  $p$  and on the polynomial  $P(d)$  used to define the rational degradation function given in (9)–(10). The quadratic polynomial  $P(d)$  in (10) can capture convex and linear softening responses but it is insufficient to capture concave softening responses. Therefore, to successfully recast the original PPR model within the framework of the phase-field method, we need to modify the degradation function  $g(d)$  so that it can capture concave softening responses. To do so, we consider a third-order polynomial  $P(d)$ , so that Eq. (10) becomes

$$Q(d) = a_1 d \cdot P(d), \quad \text{with } P(d) = 1 + a_2 d + a_3 d^2 + a_4 d^3, \tag{30}$$

where  $a_4$  is an additional calibration parameter.

In Eq. (30), parameters  $a_1$ ,  $a_2$ , and  $a_3$  are obtained following the same procedure described previously (see also (Wu, 2017)). Parameters  $a_1$  and  $a_2$  remain unchanged despite the addition of  $a_4$  and can still be obtained from Eqs. (24) and (25), respectively. Parameter  $a_3$ , however, becomes dependent on the new parameter  $a_4$ . The resulting expression for  $a_3$  is as follows:

$$\delta_n := \lim_{d^* \rightarrow 1} \Delta_n(d^*) \rightarrow a_3 = \begin{cases} 0, & p > 2 \\ \frac{1}{a_2 + a_4} \left[ \frac{1}{8} \left( \frac{\delta_n \sigma_{\max}}{\phi_n} \right)^2 - (1 + a_2) \right], & p = 2. \end{cases} \tag{31}$$

<sup>7</sup> Although essential to correctly model mixed-mode fracture problems, a version of the regularized PPR model considering the general form of the extrinsic PPR model is out of the scope of this work. However, our numerical results indicate that the mode-I version of the regularized PPR model is adequate to model fracture problems with moderate mode mixity.

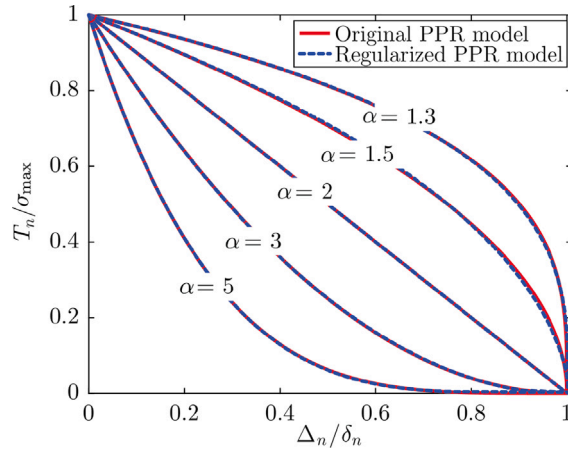


Fig. 7. Softening curves predicted by the regularized PPR model for various values of  $\alpha$ . As the results show, the regularized PPR model predicts almost identical traction–separation responses as the original PPR model for a wide range of  $\alpha$  values.

To evaluate  $a_2$  (Eq. (25)) and the new  $a_3$  (Eq. (31)) we need the initial slope,  $k_0$ , and the final crack opening,  $\delta_n$ , from the original PPR model. These are obtained directly from Eq. (29) and are given by:

$$k_0 = \left. \frac{dT_n}{d\Delta_n} \right|_{\Delta_n=0} = -\frac{(\alpha - 1)\sigma_{\max}^2}{\alpha\phi_n} \quad \text{and} \quad \delta_n = \alpha \frac{\phi_n}{\sigma_{\max}}. \tag{32}$$

Because the new parameter,  $a_4$ , is used to capture concave softening responses, it will be set to zero when  $\alpha \geq 2$ . For other values of  $\alpha$ , parameter  $a_4$  is obtained using a least-squares technique to approximate the PPR tractions given by (29) using the equivalent traction–separation relationship (22)–(23). An optimized value for  $a_4$  is obtained for a given value of  $\alpha$ , and subsequently a cubic polynomial is employed to fit the optimized  $a_4$  values as a function of  $\alpha$ . This procedure yields the following expression for  $a_4$ :

$$a_4 = \begin{cases} 0, & \alpha \geq 2 \\ -14.49\alpha^3 + 63.01\alpha^2 + 87.97\alpha + 39.86 & \alpha < 2. \end{cases} \tag{33}$$

From our experience, parameter  $p$  helps to control the shape of the softening response when  $\alpha$  takes large values. To obtain an expression for  $p$  as a function of  $\alpha$ , we adopt the same least-squares procedure employed to obtain (33). That is, parameter  $p$ , is optimized for different values of  $\alpha$  to fit the original PPR model, leading to the following cubic polynomial:

$$p = \begin{cases} 2, & \alpha \leq 2.6 \\ 7.30 \times 10^{-4}\alpha^3 - 1.96 \times 10^{-2}\alpha^2 + 1.93 \times 10^{-1}\alpha + 1.62, & \alpha > 2.6. \end{cases} \tag{34}$$

Fig. 7 compares the traction–separation curves obtained with the regularized PPR model against those from the original PPR model for different values of  $\alpha$ .<sup>8</sup> The curves from the regularized PPR model are obtained from Eqs. (22)–(23) using the polynomial  $P(d)$  from (30) with parameters  $a_1$  and  $a_2$  from Eqs. (24)–(25),  $a_3$  from Eq. (31),  $a_4$  from Eq. (33), and  $p$  from Eq. (34). As shown by the results in Fig. 7, the traction–separation curves from the regularized and the original PPR model are nearly identical.

Due to its ability to control the shape of the cohesive softening response, the regularized PPR model can also be used to reproduce or approximate some of the traction–separation laws frequently adopted in the literature. The approximation can be achieved by selecting an appropriate value for the shape parameter,  $\alpha$ , that matches the slope and the final crack opening of the target traction–separation law and calibrating the parameter  $p$ , if needed, to obtain a better approximation. To illustrate this, the linear and exponential softening responses will be recovered.

For the linear softening response we have

$$T_n(\Delta_n) = \sigma_{\max} \max \left( 1 - \frac{\sigma_{\max}}{2\phi_n} \Delta_n, 0 \right), \quad k_0 = -\frac{\sigma_{\max}^2}{2\phi_n}, \quad \text{and} \quad \delta_n = \frac{2\phi_n}{\sigma_{\max}}.$$

<sup>8</sup> Values of  $\alpha \in (1, 2)$  (concave softening response) violate the crack irreversibility condition because the initial crack bandwidth is larger than the ultimate crack bandwidth (see Wu (2017)). However, we found that the crack irreversibility condition is only slightly violated for  $\alpha \in [1.5, 2)$ . Because this range of  $\alpha$  values effectively encompasses concave softening responses for a wide range of practical applications, we recommend  $\alpha \in [1.5, 2)$  whenever concave softening responses are required.

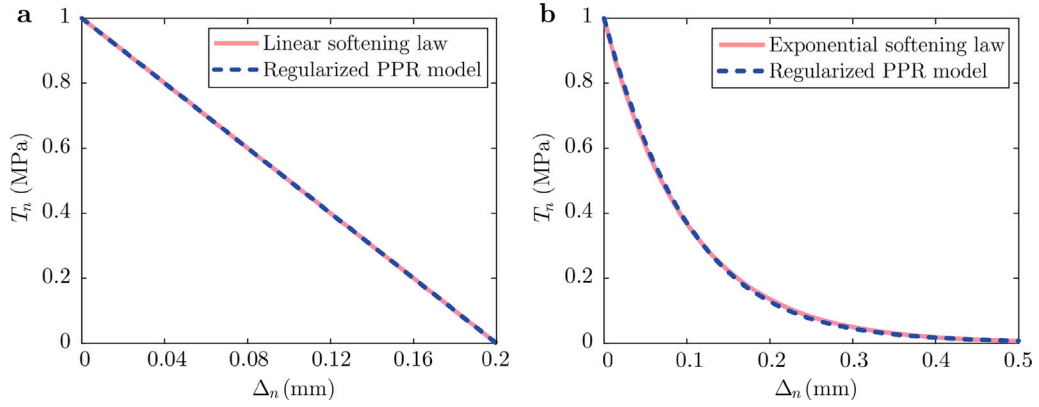


Fig. 8. Classical softening responses reproduced by the regularized PPR model: (a) linear softening ( $\alpha = 2$ ) and (b) exponential softening ( $\alpha = 15$ ). The results shown here are obtained for  $\sigma_{\max} = 1$  MPa and  $\phi_n = 0.1$  N/mm.

By comparing the slope and the final crack opening against the ones for the regularized PPR model, Eq. (32), it can be noticed that by choosing  $\alpha = 2$ , the linear traction–separation law can be exactly recovered (see Fig. 8a). For the exponential softening response, its initial slope and its final crack opening are given by

$$T_n(\Delta_n) = \sigma_{\max} \exp\left(-\frac{\sigma_{\max}}{\phi_n} \Delta_n\right), \quad k_0 = -\frac{\sigma_{\max}^2}{\phi_n}, \quad \text{and} \quad \delta_n = +\infty.$$

Similarly, by comparing these equations with Eq. (32) it can be noticed that the greater  $\alpha$  is, the closer the initial slope and the final crack opening are to those from the exponential model. In fact, by comparing Eq. (32) with the equations above, one can prove that when  $\alpha \rightarrow \infty$  the initial slope and the final crack opening can be exactly recovered (see Fig. 8b).

### 5. Finite element implementation

The governing balance equations (12) and (20) are solved via the finite element method. The weak form of the governing balance equations are given by

$$\int_{\Omega} g(d) \bar{\boldsymbol{\sigma}} : \delta \boldsymbol{\varepsilon} \, dV - \int_{\Omega} \mathbf{f} \cdot \delta \mathbf{u} \, dV - \int_{\partial \Omega_t} \mathbf{t} \cdot \delta \mathbf{u} \, dS = 0 \tag{35}$$

and

$$\int_{\Omega} \frac{\phi_n}{c_0 l_0} \left[ \omega'(d) \delta d + l_0^2 \nabla d \cdot \delta \nabla d \right] \, dV + \int_{\Omega} g'(d) \mathcal{H} \delta d \, dV = 0, \tag{36}$$

respectively.

The domain  $\Omega$  is discretized into  $N_e$  finite elements,  $\{\Omega_e\}_{e=1}^{N_e}$ . Within each finite element, the displacement field  $\mathbf{u}$  and the phase field  $d$  are respectively approximated using the element nodal displacement vector,  $\mathbf{u}^e$ , and the nodal phase-field vector,  $\mathbf{d}^e$ , as follows:

$$\mathbf{u} = \mathbf{N}_u \mathbf{u}^e, \quad d = \mathbf{N}_d \mathbf{d}^e, \tag{37}$$

where  $\mathbf{N}_u$  and  $\mathbf{N}_d$  are given by:

$$\mathbf{N}_u = \begin{bmatrix} N_1 & 0 & \dots & N_N & 0 \\ 0 & N_1 & \dots & 0 & N_N \end{bmatrix} \quad \text{and} \quad \mathbf{N}_d = [N_1 \quad \dots \quad N_N], \tag{38}$$

where  $N_1, \dots, N_N$  are the one-dimensional shape functions and  $N$  is the number of nodes per element.<sup>9</sup> The infinitesimal strain vector and the gradient of the phase-field within an element are obtained as:

$$\boldsymbol{\varepsilon} = \mathbf{B}_u \mathbf{u}^e \quad \text{and} \quad \nabla d = \mathbf{B}_d \mathbf{d}^e, \tag{39}$$

respectively, where

$$\mathbf{B}_u = \begin{bmatrix} N_{1,x} & 0 & \dots & N_{N,x} & 0 \\ 0 & N_{1,y} & \dots & 0 & N_{N,y} \\ N_{1,y} & N_{1,x} & \dots & N_{N,y} & N_{N,x} \end{bmatrix} \quad \text{and} \quad \mathbf{B}_d = \begin{bmatrix} N_{1,x} & \dots & N_{N,x} \\ N_{1,y} & \dots & N_{N,y} \end{bmatrix}. \tag{40}$$

<sup>9</sup> In our implementation, we consider linear triangular elements, such that  $N = 3$ .

Here,  $N_{i,x}$  and  $N_{i,y}$ ,  $i = 1, \dots, N$ , refer to the partial derivatives of the shape functions with respect to  $x$  and  $y$ , respectively. We use the same discretization for the test functions, such that:

$$\delta \mathbf{u} = \mathbf{N}_u \delta \mathbf{u}^e, \quad \delta d = \mathbf{N}_d \delta \mathbf{d}^e, \quad \delta \boldsymbol{\varepsilon} = \mathbf{B}_u \delta \mathbf{u}^e, \quad \delta \nabla d = \mathbf{N}_d \delta \mathbf{d}^e \quad (41)$$

where  $\delta \mathbf{u}^e$  and  $\delta \mathbf{d}^e$  are vectors containing nodal values of the test functions.

After applying the aforementioned discretization, the weak form (35)–(36) can be written (at the element level) as

$$(\delta \mathbf{u}^e)^T \left[ \int_{\Omega_e} \mathbf{B}_u^T g(d) \mathbf{D}_e \mathbf{B}_u dV \right] \mathbf{u}^e - (\delta \mathbf{u}^e)^T \left[ \int_{\Omega_e} \mathbf{N}_u^T \mathbf{f} dV + \int_{\partial \Omega_e^e} \mathbf{N}_u^T \mathbf{t} dS \right] = 0 \quad (42)$$

$$(\delta \mathbf{d}^e)^T \left[ \int_{\Omega_e} \mathbf{B}_d^T \left( \frac{2l_0 \phi_n}{c_0} \right) \mathbf{B}_d dV \right] \mathbf{d}^e + (\delta \mathbf{d}^e)^T \left[ \int_{\Omega_e} \mathbf{N}_d^T \left( g'(d) \mathcal{H} + \frac{\phi_n}{c_0 l_0} \omega'(d) \right) dV \right] = 0 \quad (43)$$

where  $\mathbf{D}_e$  is the tangent modulus matrix. For the displacement field, Eq. (42) results in the discretized weak form:

$$\underbrace{\left[ \int_{\Omega_e} \mathbf{B}_u^T g(d) \mathbf{D}_e \mathbf{B}_u dV \right]}_{\mathbf{F}_u^{\text{int}}} \mathbf{u}^e = \underbrace{\int_{\Omega_e} \mathbf{N}_u^T \mathbf{f} dV + \int_{\partial \Omega_e^e} \mathbf{N}_u^T \mathbf{t} dS}_{\mathbf{F}_u^{\text{ext}}}, \quad (44)$$

where the left-hand side of (44) represents the element internal force vector,  $\mathbf{F}_u^{\text{int}}$ , and the right-hand side represents the element external force vector,  $\mathbf{F}_u^{\text{ext}}$ . For the phase-field, Eq. (43) results in the discretized weak form (at the element level):

$$\underbrace{\left[ \int_{\Omega_e} \mathbf{B}_d^T \left( \frac{2l_0 \phi_n}{c_0} \right) \mathbf{B}_d dV \right]}_{\mathbf{F}_d^{\text{int}}} \mathbf{d}^e + \left[ \int_{\Omega_e} \mathbf{N}_d^T \left( g'(d) \mathcal{H} + \frac{\phi_n}{c_0 l_0} \omega'(d) \right) dV \right] = 0, \quad (45)$$

where the left-hand side of (45) represents the internal force vector of the phase field,  $\mathbf{F}_d^{\text{int}}$ , and the right-hand side represents the external force vector,  $\mathbf{F}_d^{\text{ext}} = 0$ . The element stiffness matrix for the displacement field and the element tangent matrix for the phase-field are obtained, respectively, as

$$\mathbf{k}_u^e = \frac{\partial \mathbf{F}_u^{\text{int}}}{\partial \mathbf{u}^e} \quad \text{and} \quad \mathbf{k}_d^e = \frac{\partial \mathbf{F}_d^{\text{int}}}{\partial \mathbf{d}^e}. \quad (46)$$

which results in the following local element matrices for the FE implementation:

$$\mathbf{k}_u^e = \int_{\Omega_e} \left[ \mathbf{B}_u^T g(d) \mathbf{D}_e \mathbf{B}_u \right] dV, \quad (47)$$

$$\mathbf{k}_d^e = \int_{\Omega_e} \left[ \mathbf{B}_d^T \left( \frac{2\phi_n l_0}{c_0} \right) \mathbf{B}_d + \mathbf{N}_d^T \left( g''(d) \mathcal{H} + \frac{\phi_n}{c_0 l_0} \omega''(d) \right) \mathbf{N}_d \right] dV. \quad (48)$$

The element equations (44)–(48) can be assembled in a standard form to solve the displacement and phase-field problems on the entire domain,  $\Omega$ . The global stiffness matrix and the tangent matrix are obtained as:

$$\mathbf{K}_u = \sum_{e=1}^{N_e} \mathbf{k}_u^e \quad \text{and} \quad \mathbf{K}_d = \sum_{e=1}^{N_e} \mathbf{k}_d^e, \quad (49)$$

where  $\Sigma$  refers to the FE assembly operator.

Given that we are implementing the hybrid formulation (Ambati et al., 2015), the displacement problem is linear and it can be solved directly in each time step. Conversely, the phase-field problem is nonlinear and needs to be solved iteratively via the Newton–Raphson method. The implementation of the regularized PPR model follows the schematic flowchart shown in Fig. 9 and the pseudocode shown in Algorithm 1. The first step is to read all necessary input data, including the finite element discretization and boundary conditions, material properties, model parameters (length scale,  $l_0$ , and shape parameter,  $\alpha$ ), and convergence tolerances. Using the provided input data, the next step is to compute the calibration parameters  $a_1$ ,  $a_2$ ,  $a_3$ ,  $a_4$ , and  $p$  using Eqs. (24), (25), (31), (33), and (34), respectively. Once the calibration parameters have been obtained, the next step is to use the Newton–Raphson method to solve the phase-field problem defined using Eq. (45) until some convergence criteria are satisfied. Once the phase-field problem has reached convergence, the next step is to solve the displacement problem defined using Eq. (44).<sup>10</sup> Finally, the history field,  $\mathcal{H}$ , is updated with the phase-field and displacement field values obtained at the current time step.

<sup>10</sup> Given that the element equation (44) is linear, the displacement problem can be solved in a single Newton–Raphson iteration.

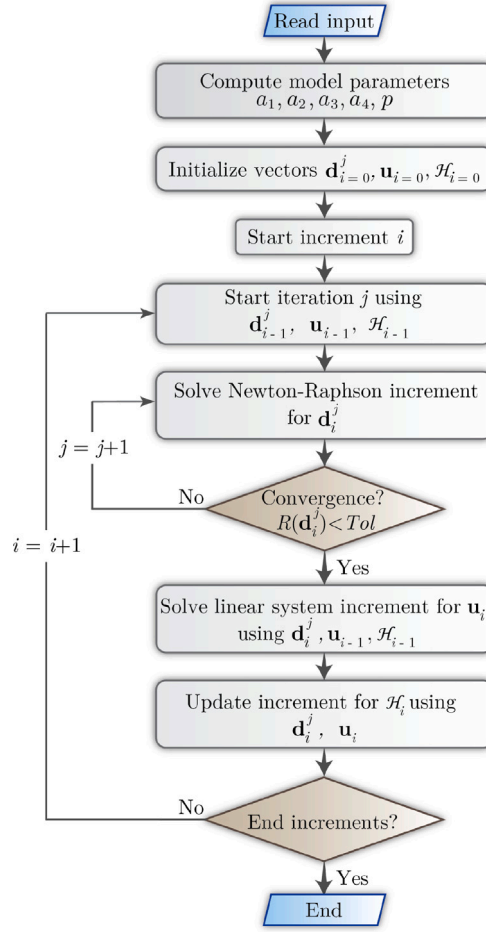


Fig. 9. Flowchart for the implemented staggered solution.

**Algorithm 1** Staggered scheme for the regularized PPR model

- 1: **input:** Load data: Finite element mesh and boundary conditions  
Material parameters:  $E$ ,  $\nu$ ,  $\phi_n$ ,  $\sigma_{\max}$   
Model parameters:  $l_0$ ,  $\alpha$   
Convergence tolerance and number of load steps: Tol and  $N_{\text{steps}}$
- 2: **evaluate:**  $a_1$ ,  $a_2$ ,  $a_3$ ,  $a_4$ , and  $p$  from (24), (25), (31), (33), and (34), respectively
- 3: **initialize:**  $j = 0$ ,  $\mathbf{d}_0 = \mathbf{0}$ ,  $\mathbf{u}_0 = \mathbf{0}$ , and  $\mathcal{H}_0$  using Eq. (21)
- 4: **for**  $i = 1$  to  $N_{\text{steps}}$  **do** ▷ Loop over load/displacement steps
- 5:   Set  $j = 0$ ,  $\mathbf{d}_i^j = \mathbf{d}_{i-1}$ , and  $\text{Err} = 10 \times \text{Tol}$
- 6:   **while**  $\text{Err} > \text{Tol}$  **do** ▷ Newton-Raphson iterations
- 7:     Evaluate geometric function  $\omega(\mathbf{d}_i^j)$  using Eq. (8)
- 8:     Evaluate degradation function  $g(\mathbf{d}_i^j)$  using Eqs. (9) and (30)
- 9:     Obtain phase-field increment,  $\Delta \mathbf{d}_i^j$ , by solving  $\mathbf{K}_d(\mathbf{d}_i^j) \Delta \mathbf{d}_i^j = -\mathbf{F}_d^{\text{int}}(\mathbf{d}_i^j)$ , with  $\mathbf{K}_d(\mathbf{d}_i^j)$  from (49) and  $\mathbf{F}_d^{\text{int}}(\mathbf{d}_i^j)$  assembled from (45)
- 10:    Update phase-field:  $\mathbf{d}_i^{j+1} = \mathbf{d}_i^j + \Delta \mathbf{d}_i^j$
- 11:    Obtain displacement vector,  $\mathbf{u}_i$ , by solving  $\mathbf{K}_u \mathbf{u}_i = \mathbf{F}_u^{\text{ext}}$ , with  $\mathbf{K}_u$  from (49)
- 12:    Update history field  $\mathcal{H}_i$  using Eq. (21)
- 13:    Evaluate norm of phase-field residual:  $\text{Err} = \|\mathbf{F}_d^{\text{int}}(\mathbf{d}_i^{j+1})\|$
- 14:    Update iteration counter:  $j \leftarrow j + 1$
- 15:   **end while**
- 16:   **output:**  $\mathbf{d}_i \leftarrow \mathbf{d}_i^j$  and  $\mathbf{u}_i$
- 17: **end for**

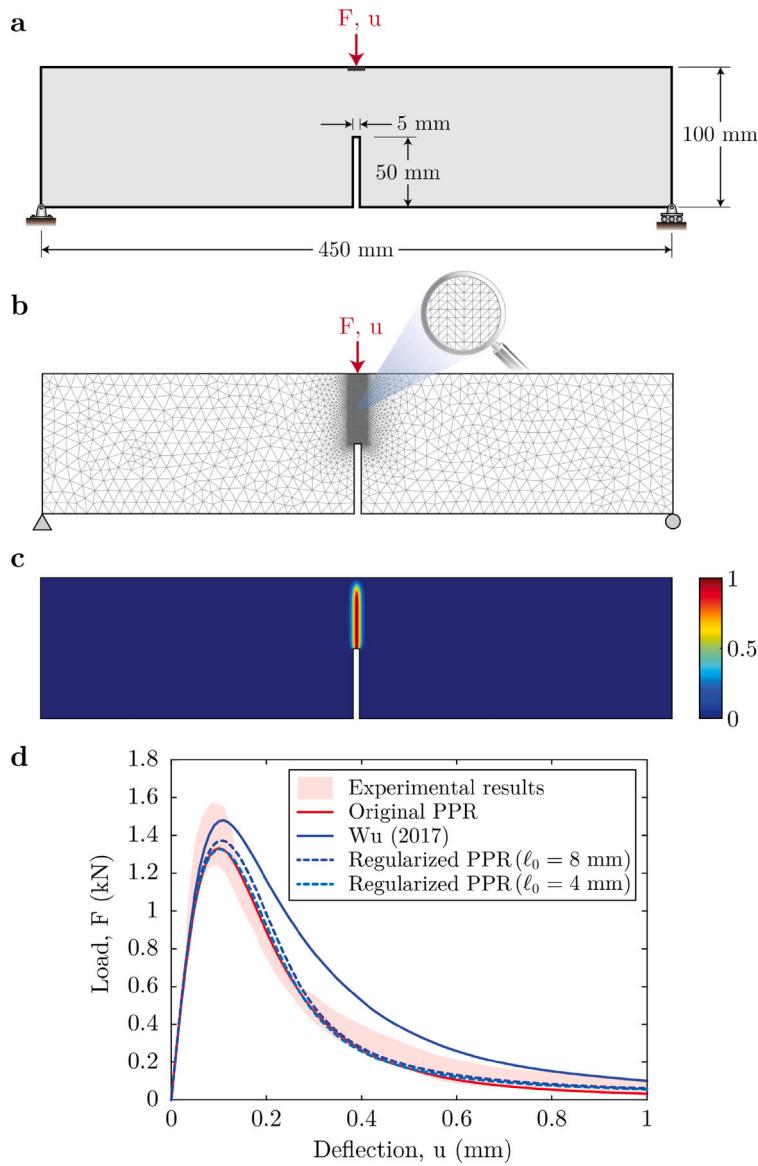


Fig. 10. Three-point bending of a notched concrete beam: (a) domain and boundary conditions, (b) finite element mesh, (c) crack path predicted by the regularized PPR model with  $l_0 = 8$  mm, and (d) load vs. deflection curves.

## 6. Results and discussion

Here we discuss several representative examples that demonstrate the ability of the regularized PPR model to simulate quasi-brittle fracture problems. For each example, we compare the obtained load–deflection curves with those from other phase-field formulations and with experimental results. In addition, the crack path obtained with the regularized PPR model is compared, when available, against those reported experimentally.

All numerical computations are obtained using a displacement-controlled finite element implementation of the regularized PPR model with constant displacement increments. Plane stress conditions are used to solve the problems unless otherwise specified. Problems in which the crack path can be easily predicted are also modeled with the original PPR model.<sup>11</sup> In order to ensure an accurate prediction of the fracture energy in the discrete context and to ensure that the numerical solution adequately resolves

<sup>11</sup> The FE implementation used to solve problems where the crack path is known a priori is based on the thermodynamically consistent intrinsic PPR model (Spring et al., 2016).

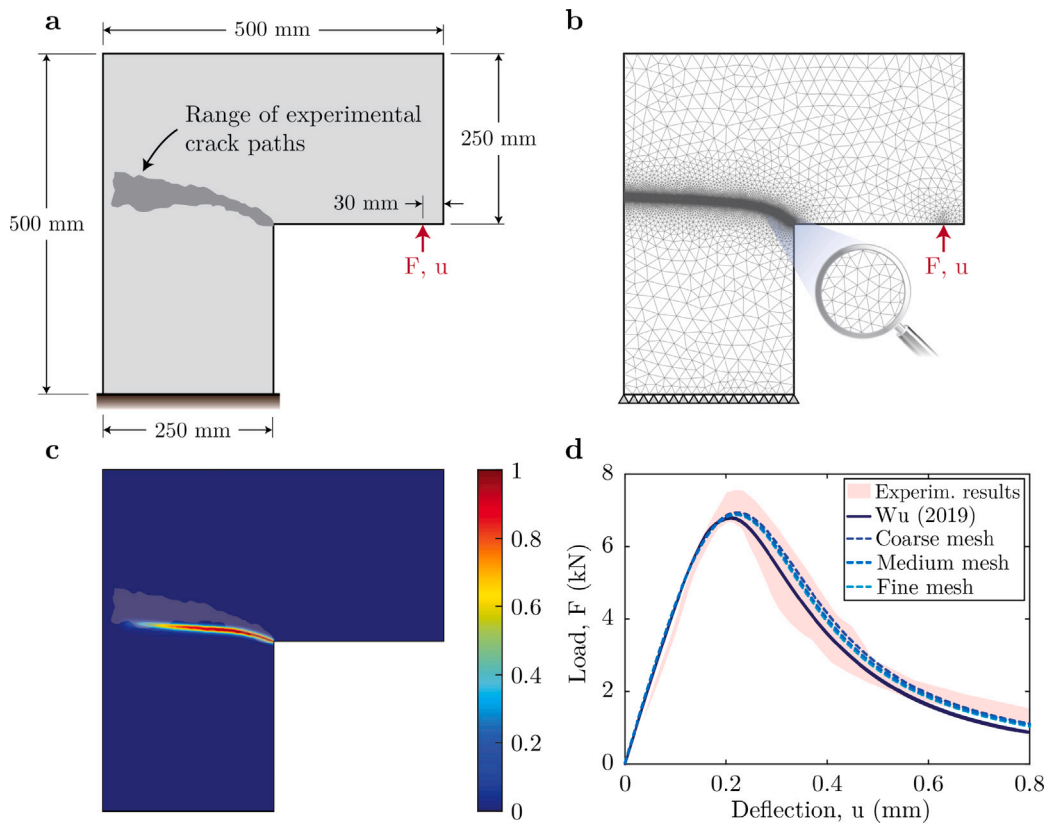


Fig. 11. Fracture modeling of an L-shaped concrete panel: (a) domain and boundary conditions, (b) finite element mesh (coarse), (c) crack path predicted by the regularized PPR model with  $l_0 = 5$  mm, and (d) load vs. deflection curves.

the phase-field gradient, for most of the problems we adhere to a general rule where we choose the length scale,  $l_0$ , such that the element size in the critical zone satisfies  $h \leq l_0/5$ .

### 6.1. Mode-I fracture of a three-point bending beam

In this example, we use the regularized PPR model to simulate a three-point bending test on the notched concrete beam reported by Rots (1988) whose geometry is shown in Fig. 10a. The beam has an out-of-plane thickness of 100 mm and it is discretized using 9,054 linear triangular elements, such that the effective element size is  $h \approx 0.50$  mm in the critical zone and  $h \approx 10$  mm far from it, as shown in Fig. 10b. The beam is made of concrete with Young's modulus  $E_0 = 2.0 \times 10^4$  MPa and Poisson's ratio  $\nu = 0.2$  (Rots, 1988). The fracture parameters used to solve this problem were obtained via inverse analysis to improve the approximation of the experimental load–deflection curves (Shen and Paulino, 2011b,a; Hill et al., 2017). The calibrated fracture parameters are  $\phi_n = 0.078$  N/mm,  $\sigma_{\max} = 2.04$  MPa, and  $\alpha = 4$ . For this problem, we obtain numerical results using two different length-scale parameters ( $l_0 = 4$  mm and 8 mm) and constant displacement increments of  $\Delta u_y = 5 \times 10^{-4}$  mm.

Figs. 10c–d show the numerical results obtained with the regularized PPR model. Fig. 10c illustrates the crack path obtained with the regularized PPR model for  $l_0 = 8$  mm. It can be observed that the model predicts a vertical crack path (as expected) without any additional crack-tracking strategy. Fig. 10d compares the numerical and experimental load–deflection curves. Fig. 10d shows the load–deflection curves obtained with the regularized PPR model for  $l_0 = 4$  mm and  $l_0 = 8$  mm as well as the load–deflection curve obtained with the original PPR model and that reported by Wu (2017). As observed in the figure, the numerical load–deflection curves obtained with the regularized PPR model are in good agreement with the experimental curves reported by Rots (1988). Moreover, we observe that the load–deflection curves are slightly affected by  $l_0$  and the results approach those obtained with the original PPR model as  $l_0$  decreases.<sup>12</sup> This last observation is valid since the smeared crack approaches a sharp crack as  $l_0$  tends to zero.

<sup>12</sup> Although our model is somewhat sensitive to the length scale parameter  $l_0$ , Fig. 10 nonetheless shows that the results are still very similar for a wide range of values of this parameter.

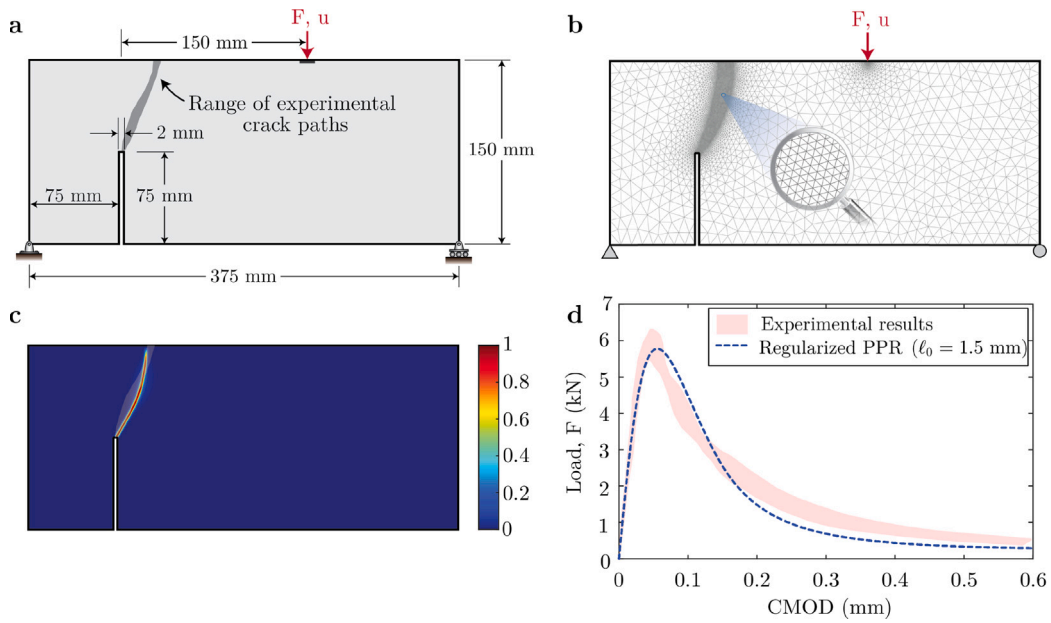


Fig. 12. Mixed-mode fracture modeling of an eccentrically notched beam under three point bending: (a) domain and boundary conditions, (b) finite element mesh, (c) crack path predicted by the regularized PPR model with  $l_0 = 1.5$  mm, and (d) load vs. deflection curves.

## 6.2. Mixed-mode fracture of an L-shaped panel

In this example, we consider the mixed-mode fracture of an L-shaped panel with geometry and boundary conditions shown in Fig. 11a. The geometry, loading, material parameters, and experimental results are adopted from Winkler (2001). The out-of-plane thickness of the L-panel is 100 mm and it is made of concrete with Young's modulus  $E_0 = 2.0 \times 10^4$  MPa and Poisson's ratio  $\nu = 0.18$ .<sup>13</sup> The fracture parameters used for the regularized PPR model are  $\phi_n = 0.130$  N/mm,  $\sigma_{\max} = 2.5$  MPa, and  $\alpha = 7$ . The calibrated cohesive strength adopted in the simulations is 20% lower than that reported by Unger et al. (2007) and the fracture energy is 5% lower. A calibrated cohesive strength is used to bring the simulated results into reasonable comparison with the experimental results, as suggested by Song et al. (2006).

To solve this problem, we use  $l_0 = 5$  mm and consider three mesh sizes (i.e., coarse, medium, and fine), where each mesh is composed of linear triangular elements which become refined in the critical zone where the crack is expected to propagate (Fig. 11b). The element size in the critical region is  $h \approx 1.0$  mm for the first mesh (coarse),  $h \approx 0.50$  mm for the second mesh (medium), and  $h \approx 0.25$  mm for the third mesh (fine) and the element size outside the critical region is  $h \approx 20$  mm for each of the three meshes. The computations were performed using constant displacement increments of  $\Delta u_y = 1.0 \times 10^{-4}$  mm at the point of load application (see Fig. 11a-b).

Fig. 11c shows the crack path predicted by the regularized PPR model with the coarse mesh. These results show that the regularized PPR model can reasonably capture the curved crack paths reported experimentally.<sup>14</sup> Finally, Fig. 11d compares the numerical load–deflection curves obtained with the regularized PPR model against those reported by Wu et al. (2019), and against those obtained experimentally by Winkler (2001). As the results indicate, the load–deflection curves obtained with the regularized PPR model closely resemble those reported experimentally. Additionally, when comparing the results from the coarse, medium, and fine meshes in Fig. 11d, it is clear that our finite element results converge under mesh refinement.

## 6.3. Mixed-mode fracture of a three-point bending beam

In this example, we consider a beam with an eccentric notch and load undergoing three-point bending. For this problem, we use the experimental results reported by Gálvez et al. (1998). The geometry and boundary conditions are shown in Fig. 12a. The beam has an out-of-plane thickness of 50 mm, and it is discretized using 12,893 linear triangular elements with an effective element size of  $h \approx 0.30$  mm in the critical zone and  $h \approx 10$  mm far from it (Fig. 12b). The beam is made of concrete with Young's modulus  $E_0 = 3.8 \times 10^4$  MPa and Poisson's ratio  $\nu = 0.2$  (Zhang et al., 2018). The fracture parameters used for the regularized PPR model are

<sup>13</sup> To obtain the numerical results, here we adopt the material parameters reported by Unger et al. (2007), but modify the Young's modulus to better estimate the initial slope reported in the experiments (Fig. 11d).

<sup>14</sup> The range of experimental crack paths for this problem is depicted in both Fig. 11a and Fig. 11c.

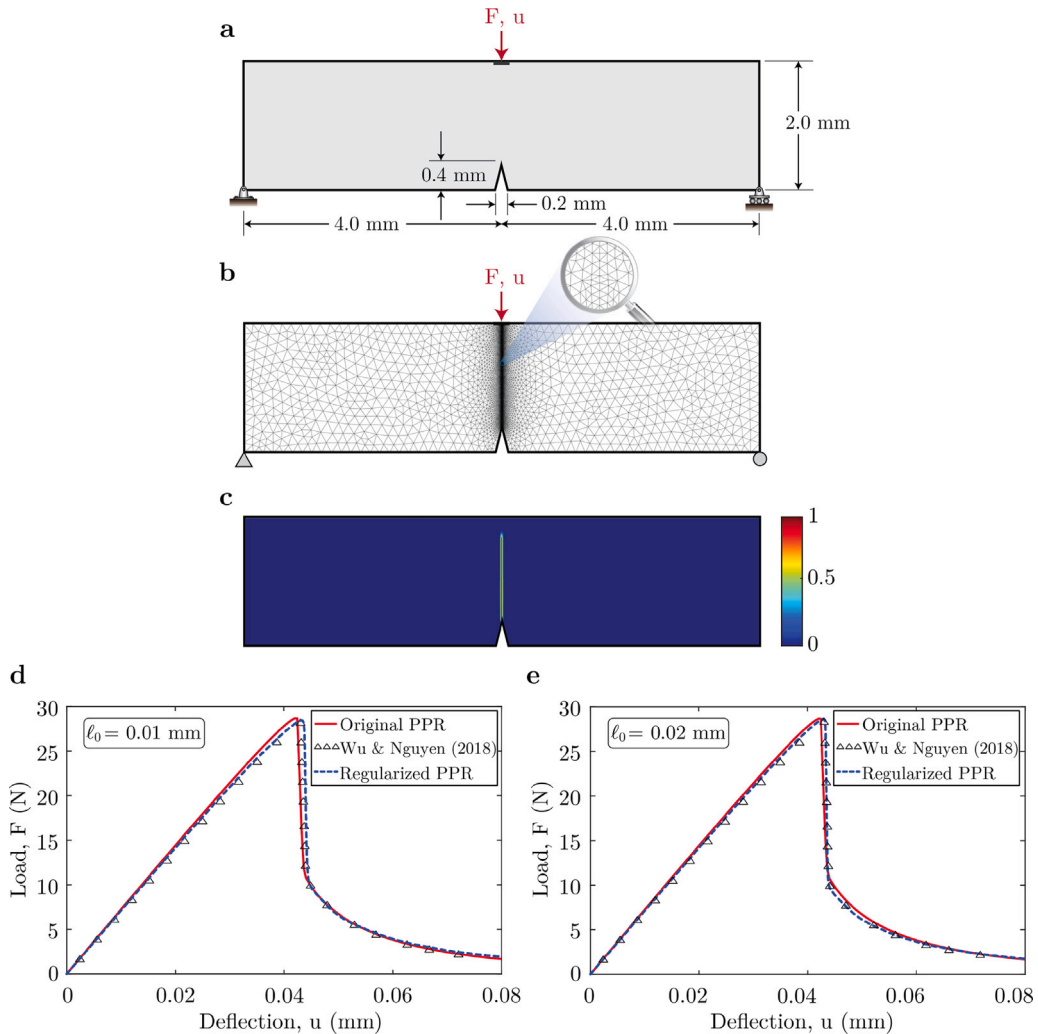


Fig. 13. Fracture modeling of a symmetrically notched beam under three-point bending (brittle fracture): (a) domain and boundary conditions, (b) finite element mesh, (c) crack path predicted by the regularized PPR model with  $l_0 = 0.01$  mm, and (d-e) load vs. deflection curves obtained with  $l_0 = 0.01$  mm and  $l_0 = 0.02$  mm, respectively.

$\phi_n = 0.069$  N/mm,<sup>15</sup>  $\sigma_{\max} = 3.0$  MPa, and  $\alpha = 4$ . Finally, we use  $l_0 = 1.5 \sigma_{\max}$  and solve the problem by applying constant displacement increments of  $\Delta u_y = 0.5 \times 10^{-4}$  mm.

The range of experimental crack paths is shown in Fig. 12a and the numerical crack path obtained with the regularized PPR model is shown in Fig. 12c. As the results show, the crack path predicted numerically closely resembles the range of experimental crack paths reported by Gálvez et al. (1998), highlighting the ability of the regularized PPR model to capture curved crack paths for problems under mixed-mode loading. In addition, Fig. 12d compares the load–CMOD (crack mouth opening displacement) curve obtained with the regularized PPR model against the range of experimental load–CMOD curves reported by Gálvez et al. (1998). As shown by these results, the regularized PPR model provides relatively accurate predictions of the experimental load–CMOD curves.

#### 6.4. Symmetric three point bending test (brittle)

In this example, we use the regularized PPR model to simulate a symmetrically notched beam under three-point bending. This example has been widely employed to verify phase-field models for brittle fracture (Miehe et al., 2010b). The test consists of a rectangular beam with a triangular notch at the middle of the bottom surface. The geometry and boundary conditions are displayed

<sup>15</sup> The fracture energy we use to obtain the numerical results is 10% smaller than that reported by Zhang et al. (2018).

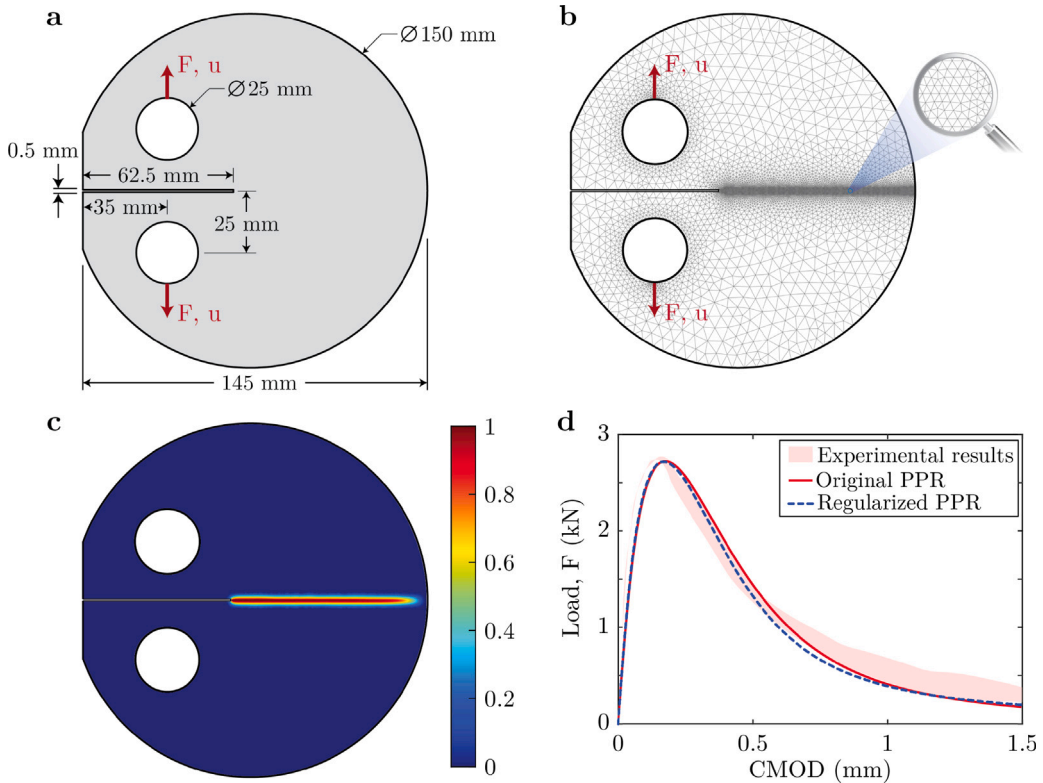


Fig. 14. Fracture modeling of a disk-shaped compact tension (DC(T)) specimen: (a) domain and boundary conditions, (b) finite element mesh, (c) crack path predicted by the regularized PPR model, and (d) load vs. CMOD curves.

in Fig. 13a. The beam is discretized using 23,014 linear triangular elements with a refinement in the critical zone, such that the effective element size in that zone is  $h \approx 0.002$  mm and  $h \approx 0.085$  mm far from it (Fig. 13b). The beam is made of concrete with Young's modulus  $E_0 = 2.08 \times 10^4$  MPa and Poisson's ratio  $\nu = 0.3$  (Wu, 2018). For this problem, we choose  $\beta_c = 100$  (cf. Eq. (18)) so the strain energy is mainly driven by  $\bar{\sigma}_1$ . The fracture parameters used for the regularized PPR model are  $\phi_n = 0.54$  N/mm,  $\sigma_{\max} = 200$  MPa, and  $\alpha = 2$ .<sup>16</sup> For this problem, we obtained numerical results for  $l_0 = 0.01$  mm and 0.02 mm. The computations are performed following Miehe et al. (2010b), that is, using constant displacement increments of  $\Delta u_y = 1.0 \times 10^{-6}$  mm for the first 360 loading steps and  $\Delta u_y = 1.0 \times 10^{-4}$  mm for the subsequent loading steps.

Figs. 13c-e show the numerical results obtained with the regularized PPR model. From Fig. 13c, we note that the model predicts a vertical crack that nucleates at the notch tip and develops vertically toward the top surface (as expected). Fig. 13d-e compares the numerical load–deflection curves obtained with the regularized PPR model against those reported by Miehe et al. (2010b) and by Wu and Nguyen (2018), and against that obtained with the original PPR model. As the results indicate, the load–deflection curves obtained with the regularized PPR model are nearly identical to those reported by Miehe et al. (2010b) and by Wu and Nguyen (2018), and to that obtained with the original PPR model. Finally, when comparing Figs. 13d and 13e one can observe that, as  $l_0$  decreases, the load–deflection curves from the regularized PPR model approach the load–deflection curve from the original PPR model.

### 6.5. Disk-shaped compact tension test

Here, we use the regularized PPR model to simulate a disk-shaped compact tension (DC(T)) test. The geometry and dimensions of the DC(T) test sample are taken from Song et al. (2006) (see Fig. 14a). The out-of-plane thickness of the DC(T) test specimen is 50 mm, and it is discretized using 16,948 linear triangular elements, such that the effective element size is  $h \approx 0.25$  mm in the critical zone and  $h \approx 5$  mm far from it (Fig. 14b). The DC(T) test sample is made of asphalt concrete with Young's modulus,  $E_0 = 14.2 \times 10^3$  MPa and Poisson's ratio  $\nu = 0.35$  (Song et al., 2006). The fracture parameters used to solve this problem are  $\phi_n = 0.328$  N/mm,  $\sigma_{\max} = 3.56$  MPa, and  $\alpha = 7$ . For this problem, we obtain numerical results using  $l_0 = 2.5$  mm and constant displacement increments of  $\Delta u_y = 1 \times 10^{-4}$  mm.

<sup>16</sup> Here we use  $\alpha = 2$  to recover the linear softening response used by Wu and Nguyen (2018).

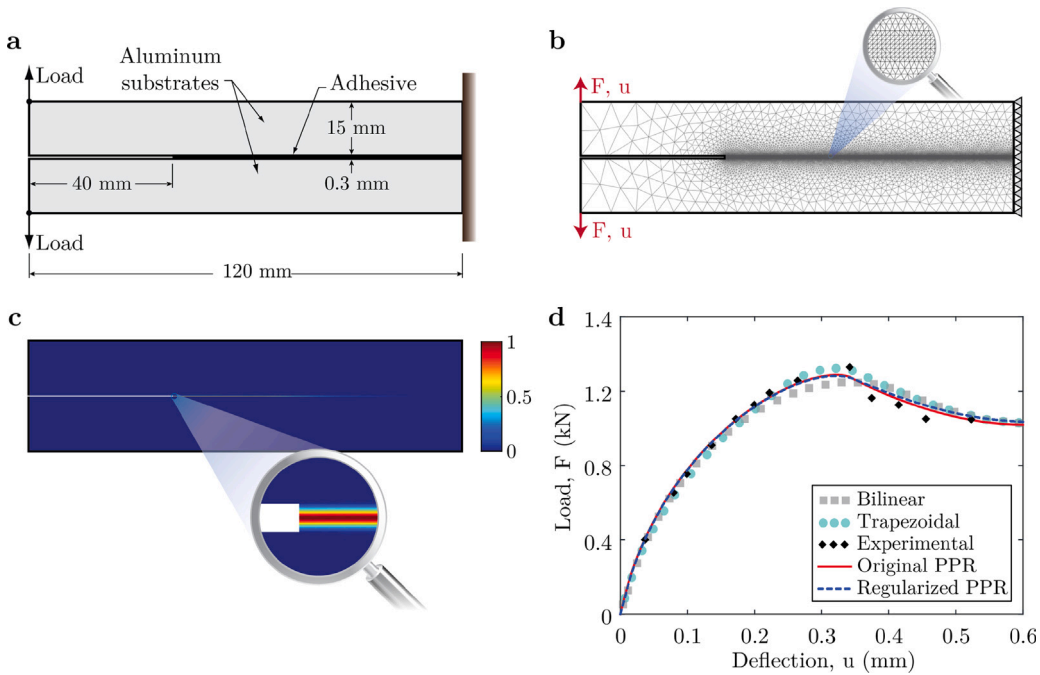


Fig. 15. Fracture modeling of a double cantilever beam (DCB): (a) domain and boundary conditions, (b) finite element mesh, (c) crack path predicted by the regularized PPR model, and (d) load vs. deflection curves.

The resulting crack path and load–CMOD (crack mouth opening displacement) curve obtained with the regularized PPR model are shown in Figs. 14c and d, respectively. Fig. 14c shows that the regularized PPR model predicts a horizontal crack path that develops along the symmetric center line, as expected. Fig. 14d compares the load–CMOD curves obtained numerically with the regularized PPR model and the original PPR model against those obtained experimentally by Song et al. (2006). As observed in the figure, the results from the regularized PPR model are nearly identical to those obtained with the original PPR model. Moreover, the two curves obtained numerically are in good agreement with those obtained experimentally.

### 6.6. Double cantilever beam test

This example demonstrates the ability of the regularized PPR model to simulate fracture of quasi-brittle materials characterized by concave softening responses. Here, we consider a double cantilever beam (DCB) test and compare the numerical results obtained with the regularized PPR model against those obtained with various classical cohesive zone models (i.e., trapezoidal and bilinear),<sup>17</sup> the original PPR model, and against experimental results reported by Pirondi and Nicoletto (2000).

The geometry and boundary conditions for the DCB test are shown in Fig. 15a. The DCB test specimen consists of two substrates made of aluminum, which are partially bonded with a methacrylate adhesive interface. Each aluminium substrate is 15-mm thick, 30-mm wide, and 120-mm long, and the adhesive interface is 0.3-mm thick and 80-mm long. The configuration has a 40-mm notch measured from the left edge of the beams, as shown in Fig. 15a. The aluminium substrates are modeled using a linear elastic material with Young's modulus  $E_s = 70$  GPa and Poisson's ratio  $\nu_s = 0.33$ , whereas the adhesive layer is modeled using a linear elastic material with Young's modulus  $E_a = 880$  MPa and Poisson's ratio  $\nu_a = 0.15$ . We consider the following fracture properties:  $\phi_n = 0.523$  N/mm,  $\sigma_{\max} = 3.3$  MPa, and  $\alpha = 1.5$ .<sup>18</sup> We assign these fracture properties only to the elements within the adhesive layer, because that is where fracture is expected to propagate. For this problem, we also use  $l_0 = 0.11$  mm, such that the phase field can fully develop within the domain comprised by the adhesive layer. Moreover, we also set  $\beta_c = 13$  in Eq. (18) and use constant displacement increments of  $\Delta u_y = 1 \times 10^{-5}$  mm. Finally, we assume plane strain conditions to match the initial slope the load–deflection curves reported by Alfano et al. (2009).

In order to resolve the length scale parameter properly, the adhesive layer is discretized using 45,710 linear triangular elements, such that the effective element size is  $h \approx 0.03$  mm in this critical zone (Fig. 15b). The substrates are discretized with 44,772 linear triangular elements. The resulting crack path and load–deflection curve obtained with the regularized PPR model are shown

<sup>17</sup> The results obtained for the classical cohesive zone models are adopted from Alfano et al. (2009). Here, we emphasize that the results from Alfano et al. (2009) are based on cohesive zone models and not on phase-field models.

<sup>18</sup> Note that we are using  $\alpha < 2$  (concave softening response) for this problem. Our rationale for choosing  $\alpha < 2$  is explained in detail in the following subsection.

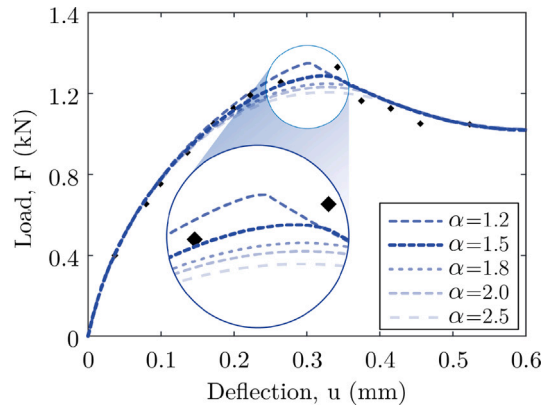


Fig. 16. Effect of the shape parameter,  $\alpha$ , on the load–deflection response for the double cantilever beam from Fig. 15.

in Fig. 15c and d, respectively. Fig. 15c shows that the crack path predicted by the regularized PPR model is located within the adhesive layer, as desired. Fig. 15d compares the numerical load–deflection curves obtained with the regularized PPR model, the original PPR model, and the bilinear and trapezoidal cohesive zone models against the experimental load–deflection curves reported by Pirondi and Nicoletto (2000). From Fig. 15d, it can be observed that the regularized PPR curve is nearly identical to the curve obtained with the original PPR model. Also, both the regularized and original PPR model results are close to the experimental ones. For the bilinear CZM, although the pre-peak response is close to the experimental one, the curve becomes more rounded close to the peak load, slightly underestimating the experimental peak load. The trapezoidal CZM is very good at capturing the peak load, but the post-peak results deviate from those obtained with the regularized PPR model (which are closer to the experimental ones).

#### 6.6.1. Shape parameter effect

Here, we discuss the effect the shape parameter has on the load–deflection curve for the DCB test discussed above. Fig. 16 shows some of the relevant results illustrating how the load–deflection curves vary when we vary  $\alpha$ . As can be observed, all the load–deflection curves are nearly identical until  $u \approx 0.15$  mm, after which the curves start to deviate depending on the value of  $\alpha$ . When the shape parameter takes small values (e.g.,  $\alpha = 1.2$ ), the response close to the peak load tends to be sharper and the peak is reached with a smaller deflection than that reported experimentally. Conversely, when  $\alpha$  takes larger values (e.g.,  $\alpha > 2$ ) the load–deflection curves tend to be more rounded close to the peak load and the predicted peak load underestimates the peak load measured experimentally. In the post-peak regime, when the deflection is  $u \approx 0.4$  mm, the curves converge again and become nearly identical to one another. Focusing only on the portion of the curves close to the peak load, Fig. 16 shows that the optimal value of the shape parameter is  $\alpha = 1.5$ , which is the value we used to solve this problem, as discussed previously (cf. Fig. 15).<sup>19</sup>

#### 6.7. Size effect analysis of symmetrically notched beams

In order to accurately model fracture of quasi-brittle materials, size, shape, and boundary effects must be properly accounted for. In general, quasi-brittle materials display a fracture process zone (FPZ) whose size is significant when compared to the size of the specimen. For instance, the FPZ size in concrete is roughly equivalent to 3–6 times the maximum aggregate size (Grégoire et al., 2013). As a result, classical linear elastic fracture mechanics is no longer applicable (Bažant and Planas, 1997).

The so-called structural size effect, which results in a decrease in the nominal peak stress, occurs for geometrically identical structures when the ratio between the sizes of the FPZ and the structure varies as the structure size changes. Moreover, the size and shape of the FPZ are different when fracture initiates and propagates at a flat boundary for unnotched specimens, leading to the so-called boundary effect of the nominal peak stress (Grégoire et al., 2013). The design of engineering structures often uses material properties that are measured at the laboratory scale, and in the majority of situations, fractures nucleate and spread in the presence of boundary effects, making the aforementioned size and boundary effects of substantial practical significance (Feng and Wu, 2018).

In this example, the regularized PPR model is applied to the modeling of fracture and size effects in concrete under mode-I fracture. Here we show the ability of the model to capture Type 1 and Type 2 size effects (Hoover et al., 2013). Type 1 size effects occur in structures that have no notches nor preexisting large cracks and fail right after the initiation of a macro-crack from a smooth surface. Type 2 size effects occur when either a deep notch or a long stress-free crack has grown in a stable manner before reaching the maximum load (Hoover et al., 2013).

Here, two different three-point bending configurations of notched and unnotched concrete beams under mode-I fracture are studied. In order to regularize the sharp crack topology with adequate accuracy, the length scale parameter  $l_0$  is chosen to be equal

<sup>19</sup> Because the regularized PPR model with  $\alpha < 2$  can capture concave softening responses, it finds applicability in scenarios where trapezoidal cohesive zone models are better suited than their linear or convex counterparts.

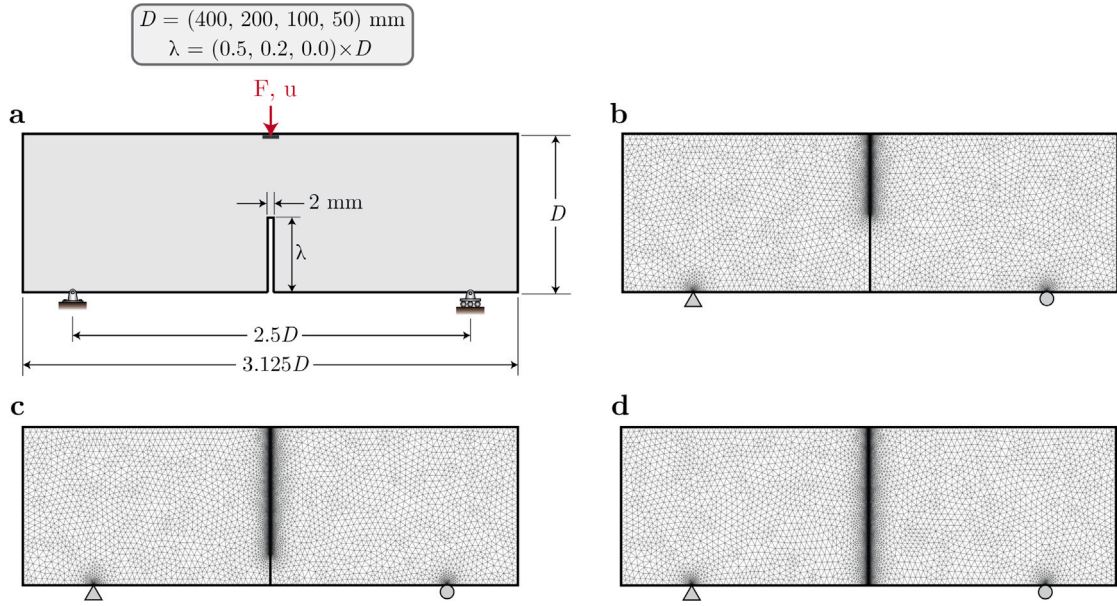


Fig. 17. Notched and unnotched three-point bending test specimens used to obtain the results shown in Fig. 18: (a) domain and boundary conditions, and finite element mesh for (b)  $\lambda = 0.5D$ , (c)  $\lambda = 0.2D$ , and (d)  $\lambda = 0.0D$ .

to  $l_0 = D/100$  in the numerical simulations, where  $D$  is the depth of the beam. Plane stress state is assumed for all the problems. The problems are crack mouth opening displacement (CMOD) controlled and when the beam is unnotched, the relative displacement between two points symmetrically located at a distance of  $D/2$  from the mid-span is used in lieu of the CMOD.

First, we discuss the case when the load and the notch are at the mid span (see Fig. 17a). The results of the models are contrasted against the data reported in Grégoire et al. (2013). As depicted in Fig. 17a, the tests consist of four different sizes of geometrically similar specimens with a span-to depth ratio of 2.5 with a depth  $D$  varying between 50 and 400 mm and a constant out-of-plane thickness of 50 mm. Three different notch-to-depth ratios are considered: 0, 0.2, and 0.5 (i.e.,  $\lambda = 0D, 0.2D$ , and  $0.5D$ , respectively, as shown in Fig. 17a), with a constant notch width of 2 mm.

The beams are discretized using linear triangular elements with a refinement in the critical zone so that the effective element size in this zone is  $h \approx l_0/10$  (Fig. 17b-d). The beams are made of concrete with Young’s modulus,  $E_0 = 3.7 \times 10^4$  MPa, Poisson’s ratio,  $\nu = 0.2$ , fracture energy,  $\phi_n = 0.10$  N/mm, cohesive strength,  $\sigma_{max} = 3.9$  MPa (Grégoire et al., 2013), and shape parameter,  $\alpha = 4$ . For this configuration, we use calibrated fractured parameters corresponding to 80% of the cohesive strength and 90% of the fracture energy reported by Grégoire et al. (2013). A constant displacement increment of  $\Delta u_y = 0.5 \times 10^{-4}$  mm is used in all the simulations.

Fig. 18 (left) shows the crack paths obtained with the regularized PPR model, which are vertical crack paths (as expected). Fig. 18 (right) compares the numerical load–CMOD responses obtained with the regularized PPR model and the original PPR model against those measured experimentally by Grégoire et al. (2013). As can be observed, the regularized PPR model and the original PPR model are able to approximate (to a certain degree of accuracy) both the post-peak softening regimes as well as the size and boundary effects affecting the peak loads.

### 6.8. Size effect analysis of eccentrically notched beams

In this example, we investigate the size effect under the transition from mode-I fracture to mixed-mode fracture by means of three-point bending tests conducted on eccentrically notched concrete beams (Fig. 17a). The numerical results are contrasted against those reported in García-Álvarez et al. (2012). Unlike the case studied in the previous example, for this new configuration either mode-I fracture or mixed-mode fracture is observed. The tests consist of three different sizes of geometrically similar specimens with a span-to depth ratio of 2.5, a depth varying between 80 and 320 mm, and a constant out-of-plane thickness of 50 mm. The notch-to-depth ratio is fixed to 0.25 (i.e.,  $a = 0.25D$ , as shown in Fig. 19a), and the eccentricity-to-depth ratio,  $e$ , is variable, while the notch width is kept constant (see Fig. 19a).

The beams are discretized using linear triangular elements with a refinement in the critical zone so that the effective element size in this zone is  $h \approx l_0/10$  (Fig. 19b-d). The beams are made of concrete with Young’s modulus,  $E_0 = 3.38 \times 10^4$  MPa, Poisson’s

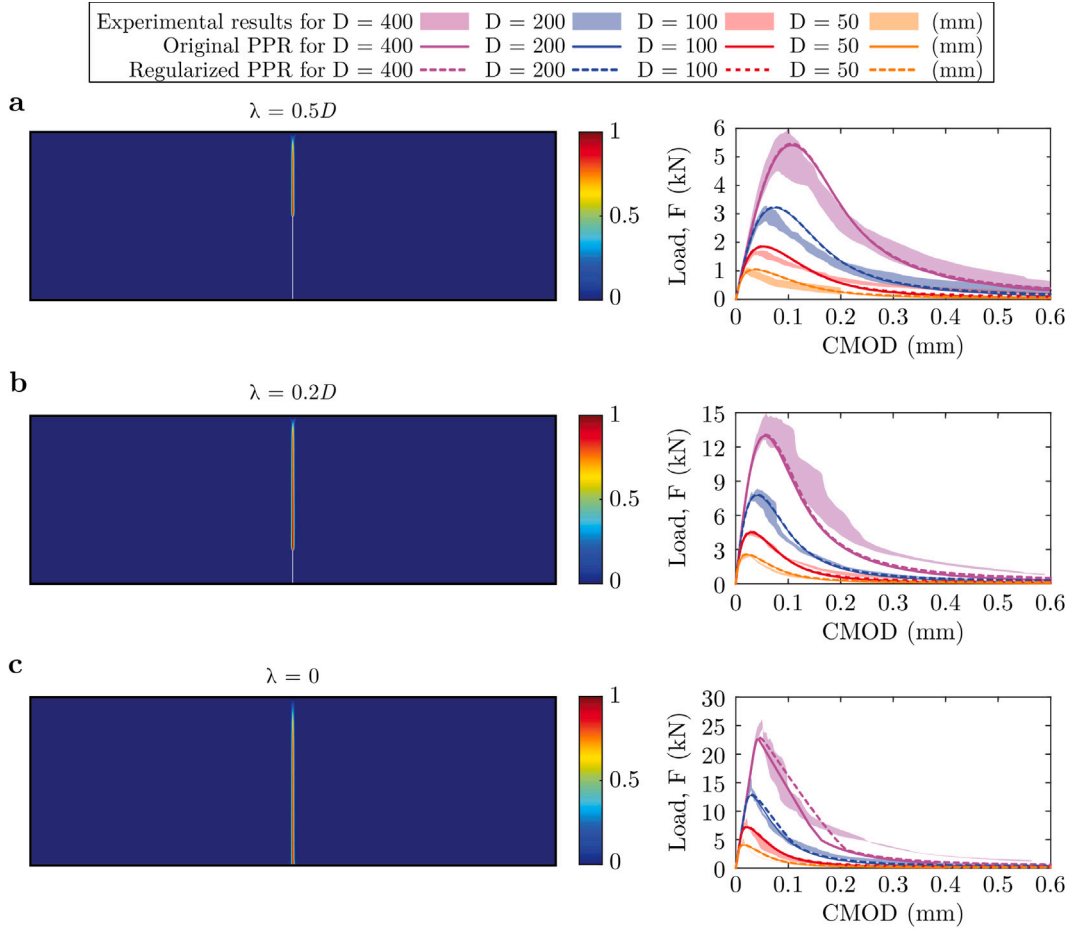


Fig. 18. Numerical vs. experimental results for the notched and unnotched beams from Fig. 17. Phase-field crack path (left) and load vs. CMOD curves (right) for: (a)  $\lambda = 0.5D$ , (b)  $\lambda = 0.2D$ , and (c)  $\lambda = 0D$ .

ratio,  $\nu = 0.2$ , fracture energy,  $\phi_n = 0.08$  N/mm, cohesive strength,  $\sigma_{max} = 3.5$  MPa (Feng and Wu, 2018), and shape parameter,  $\alpha = 4$ . For this configuration, we use calibrated fracture parameters corresponding to 90% of the cohesive strength and 90% of the fracture energy from García-Álvarez et al. (2012). A constant displacement increment of  $\Delta u_y = 0.5 \times 10^{-4}$  mm is used in all the simulations.

Fig. 20 (left) shows the resulting crack paths for the three beams and Fig. 20 (right) compares the numerical results obtained with the regularized PPR model against the experimental results reported by García-Álvarez et al. (2012). As can be observed, the agreement of the peak loads and post-peak softening regimes with a single set of material parameters is acceptable. Although the peak loads for mixed-mode are over-estimated somewhat when  $D = 320$  mm and slightly underestimated when  $D = 80$  mm or  $D = 160$  mm the difference among the results is deemed acceptable. It is also observed from Fig. 20 that the obtained numerical crack paths are consistent with the range of possible crack paths reported experimentally by García-Álvarez et al. (2012). These observations highlight the ability of the regularized PPR model to capture boundary and size effects under mixed-mode loading.

### 7. Summary and conclusions

In this work, we recast the extrinsic PPR cohesive fracture model (Park et al., 2009) within the framework of the phase-field method for quasi-brittle fracture introduced by Wu (2017). This phase-field formulation, which we refer to as the *regularized PPR model*, can reproduce cohesive softening responses of arbitrary shape (e.g., convex, concave, or linear) by means of a shape parameter inherited from the extrinsic PPR model. To achieve the desired softening response, we use a quadratic geometric function (which is amenable to phase-field formulations for quasi-brittle fracture) and a rational degradation function defined in terms of five parameters which are calibrated to reproduce the PPR softening responses.

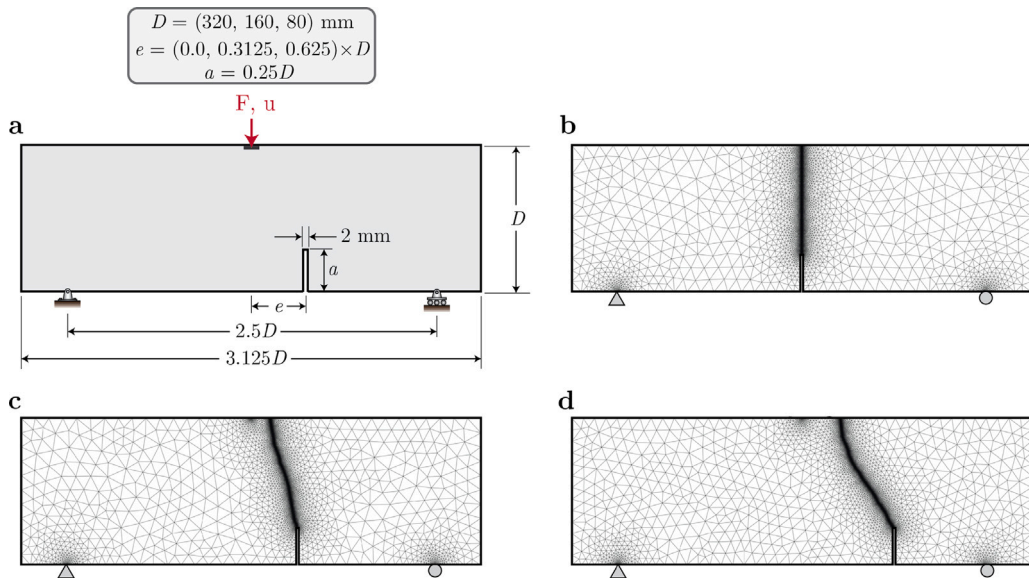


Fig. 19. Eccentrically notched beams under three-point bending used to obtain the results shown in Fig. 20: (a) domain and boundary conditions, and finite element mesh for (b)  $e = 0$ , (c)  $e = 0.3125D$ , and (d)  $e = 0.625D$ .

Illustrated with several numerical examples, we demonstrate that the regularized PPR model converges to the original PPR model as the internal length scale parameter becomes small. Moreover, we show that the crack paths and load–deflection curves predicted by the regularized PPR model are in good agreement with experimental results found in the literature. Similarly, we show that the load–deflection curves predicted by the regularized PPR model approach those predicted by the original PPR model for cases where the crack paths are known a priori. To the best of our knowledge, this is the first work in the literature where arbitrary CZM softening responses can be reproduced by a phase-field model.

Although the regularized PPR model was derived considering mode-I fracture only, the numerical results presented here suggest its efficacy for simulating mixed-mode fracture. Nonetheless, an extension of the regularized PPR model that accounts for mixed-mode fracture is needed to capture different fracture energies in modes I and II. Although such an extension is part of our future work, it is out of the scope of the present study.

### CRedit authorship contribution statement

**Rogelio A. Muñetón-López:** Performed the research, Analyzed the results, Writing – original draft. **Oliver Giraldo-Londoño:** Designed the research, Performed the research, Analyzed the results, Writing – original draft.

### Declaration of competing interest

The authors declare that they have no known competing financial interests or personal relationships that could have appeared to influence the work reported in this paper.

### Data availability

No data was used for the research described in the article.

### Acknowledgments

The authors are grateful for the endowment provided by the James W. and Joan M. O'Neill Faculty Scholar in Engineering at the University of Missouri. All authors approved the version of the manuscript to be published.

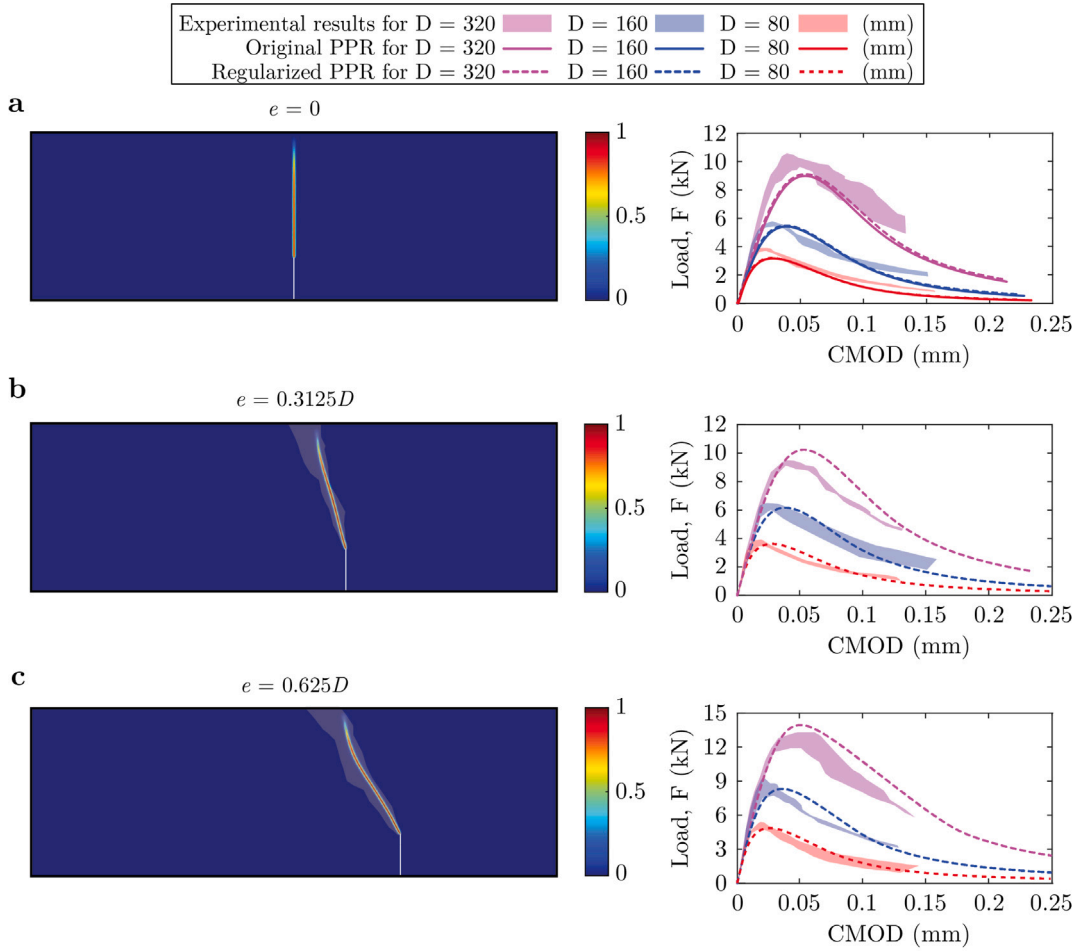


Fig. 20. Numerical vs. experimental results for the eccentrically notched beams from Fig. 19. Phase-field crack path (left) and load vs. CMOD curves (right) for: (a)  $e = 0$ , (b)  $e = 0.3125D$ , (c)  $e = 0.625D$ .

### Appendix. Nomenclature

$E_0$	Young's modulus of solid material
$T_n$	Normal cohesive traction
$Y$	Thermodynamic force that drives the evolution of the phase-field
$U$	Internal potential energy
$W_{\text{ext}}$	External potential energy
$\tilde{U}$	Regularized internal potential energy
$a_1$	Calibration parameter for the degradation function related to the material properties
$a_2$	Calibration parameter for the degradation function related to the initial slope of a traction–separation law
$a_3$	Calibration parameter for the degradation function related to the final crack opening of a traction–separation law
$a_4$	Calibration parameter related to the shape parameter $\alpha$
$c_0$	Scaling parameter of the crack surface density function
$d$	Phase-field
$f_c$	Uniaxial compressive strength
$f_t$	Uniaxial tensile strength
$g(d)$	Degradation function
$k_0$	Initial slope of a traction–separation curve
$l_0$	Length scale parameter

$p$	Exponent for the degradation function
$\Delta(\cdot)$	Laplacian operator i.e., $\Delta d = \nabla \cdot \nabla d$
$\Delta_n$	Normal crack opening displacement
$\Delta_t$	Tangential crack opening displacement
$\Gamma$	Discrete crack surface
$\Gamma_d$	Regularized crack surface
$\Gamma_n$	Energy constant for mode-I (PPR model)
$\Gamma_t$	Energy constant for mode-II (PPR model)
$\Omega$	Domain
$\Pi$	Total potential energy
$\Psi(\Delta_n, \Delta_t)$	Extrinsic PPR potential
$\alpha$	Shape parameter for mode-I fracture
$\bar{\sigma}_{\text{eq}}$	Equivalent effective stress tensor
$\bar{\Psi}$	Critical energy to obtain a zero phase-field
$\bar{\Psi}_0$	Modified initial strain energy density in terms of the equivalent effective stress
$\beta_c$	Dimensionless constant
$\beta$	Shape parameter for mode-II tractions
$\delta_n$	Final crack opening of a traction–separation law for mode-I
$\delta_s$	Dirac-delta function
$\delta_t$	Final crack opening of a traction–separation law for mode-II
$\gamma$	Crack surface density function
$\mathbb{E}_0$	Elastic stiffness tensor
$\mathcal{Y}$	Effective crack driving force
$\mathcal{H}$	Local history field of maximum strain energy
$\nabla(\cdot)$	Gradient operator
$\nu$	Poisson's ratio
$\omega(d)$	Crack function
$\partial\Omega_t$	Portion of the boundary where tractions are applied
$\partial\Omega_u$	Portion of the boundary where the system is supported
$\phi_n$	Mode-I fracture energy
$\phi_t$	Mode-II fracture energy
$\sigma_{\text{max}}$	Cohesive strength
$\psi_0$	Initial strain energy density for an isotropic elastic body
$\Psi_{\text{bulk}}$	Degrading strain energy density in the bulk
$\bar{\Pi}$	Regularized total potential energy
$\xi$	Non-negative scalar parameter for geometric function
$\bar{J}_2$	Second invariant of the deviatoric stress tensor
$\mathbf{B}^d$	Gradient operator for the phase-field
$\mathbf{B}^u$	Strain–displacement matrix for the displacement field
$\mathbf{D}$	Material tangent matrix
$\mathbf{F}_u^{\text{ext}}$	External force vector for the displacement field
$\mathbf{F}_u^{\text{int}}$	Internal force vector for the displacement field
$\mathbf{F}_d^{\text{ext}}$	External force vector for the phase-field
$\mathbf{F}_d^{\text{int}}$	Internal force vector for the phase-field
$\mathbf{K}_u$	Global stiffness matrix for the displacement field
$\mathbf{K}_d$	Global tangent matrix for the phase-field
$\mathbf{N}^d$	Interpolating shape function for the phase-field
$\mathbf{N}^u$	Interpolating shape function for the displacement field
$\mathbf{u}^e$	Element displacement vector
$\mathbf{d}^e$	Element phase-field vector
$\mathbf{f}$	Distributed body force
$\mathbf{k}_u^e$	Element stiffness matrix for the displacement field
$\mathbf{k}_d^e$	Element tangent matrix for the phase-field
$\mathbf{n}$	Outward unit normal vector to the boundary of the domain
$\mathbf{t}$	Prescribed surface tractions
$\mathbf{u}(\mathbf{x})$	Displacement field
$\bar{\sigma}$	Effective stress tensor
$\bar{\sigma}_1$	Maximum principal value of the effective stress tensor
$\sigma$	Cauchy stress tensor
$\epsilon(\mathbf{x})$	Infinitesimal strain tensor

## References

- Alfano, G., 2006. On the influence of the shape of the interface law on the application of cohesive-zone models. *Compos. Sci. Technol.* 66 (6), 723–730.
- Alfano, M., Furguieue, F., Leonardi, A., Maletta, C., Paulino, G., 2009. Mode-I fracture of adhesive joints using tailored cohesive zone models. *Int. J. Fract.* 157, 193–204.
- Ambati, M., Gerasimov, T., De Lorenzis, L., 2015. A review on phase-field models of brittle fracture and a new fast hybrid formulation. *Comput. Mech.* 55 (2), 383–405.
- Amor, H., Marigo, J.J., Maurini, C., 2009. Regularized formulation of the variational brittle fracture with unilateral contact: Numerical experiments. *J. Mech. Phys. Solids* 57 (8), 1209–1229.
- Barenblatt, G., 1959. The formation of equilibrium cracks during brittle fracture: General ideas and hypotheses, axially symmetric cracks. *J. Appl. Math. Mech.* 23 (3), 622–636.
- Bažant, Z., Oh, B., 1983. Crack band theory for fracture of concrete. *Materiaux et Constr.* 16 (3), 155–177.
- Bažant, Z., Planas, J., 1997. *Fracture and Size Effect in Concrete and Other Quasi-Brittle Materials*. Routledge.
- Borden, M.J., Hughes, T.J., Landis, C.M., Verhoosel, C.V., 2014. A higher-order phase-field model for brittle fracture: Formulation and analysis within the isogeometric analysis framework. *Comput. Methods Appl. Mech. Engrg.* 273, 100–118.
- Bourdin, B., Francfort, G.A., Marigo, J.J., 2000. Numerical experiments in revisited brittle fracture. *J. Mech. Phys. Solids* 48 (4), 797–826.
- Bourdin, B., Francfort, G.A., Marigo, J.J., 2008. The variational approach to fracture. *J. Elasticity* 91 (1), 5–148.
- Conti, S., Focardi, M., Iurlano, F., 2016. Phase field approximation of cohesive fracture models. *Annales de l'Institut Henri Poincaré C, Analyse non lineaire* 33 (4), 1033–1067.
- Dugdale, D., 1960. Yielding of steel sheets containing slits. *J. Mech. Phys. Solids* 8 (2), 100–104.
- Feng, D., Wu, J., 2018. Phase-field regularized cohesive zone model (CZM) and size effect of concrete. *Eng. Fract. Mech.* 197, 66–79.
- Francfort, G.A., Marigo, J.J., 1998. Revisiting brittle fracture as an energy minimization problem. *J. Mech. Phys. Solids* 46 (8), 1319–1342.
- Freddi, F., Iurlano, F., 2017. Numerical insight of a variational smeared approach to cohesive fracture. *J. Mech. Phys. Solids* 98, 156–171.
- Freed, Y., Banks-Sills, L., 2008. A new cohesive zone model for mixed mode interface fracture in bimetals. *Eng. Fract. Mech.* 75 (15), 4583–4593.
- Gálvez, J.C., Elices, M., Guinea, G.V., Planas, J., 1998. Mixed-mode fracture of concrete under proportional and nonproportional loading. *Int. J. Fract.* 94, 267–284.
- García-Álvarez, V., Gettu, R., Carol, I., 2012. Analysis of mixed-mode fracture in concrete using interface elements and a cohesive crack model. *Indian Acad. Sci.* 37, 187–205.
- Giraldo-Londoño, O., Paulino, G.H., Buttlar, W.G., 2019. Fractional calculus derivation of a rate-dependent PPR-based cohesive fracture model: Theory, implementation, and numerical results. *Int. J. Fract.* 216 (1), 1–29.
- Giraldo-Londoño, O., Spring, D.W., Paulino, G.H., Buttlar, W.G., 2018. An efficient mixed-mode rate-dependent cohesive fracture model using sigmoidal functions. *Eng. Fract. Mech.* 192, 307–327.
- Grégoire, D., Rojas-Solano, L., Pijaudier-Cabot, G., 2013. Failure and size effect for notched and unnotched concrete beams. *Int. J. Numer. Anal. Methods Geomech.* 37, 1434–1452.
- Griffith, A.A., 1921. The phenomena of rupture and flow in solids. *Philos. Trans. R. Soc. Lond. Ser. A* 221 (582–593), 163–198.
- Hill, B.C., Giraldo-Londoño, O., Paulino, G.H., Buttlar, W.G., 2017. Inverse estimation of cohesive fracture properties of asphalt mixtures using an optimization approach. *Exp. Mech.* 57 (4), 637–648.
- Hofacker, M., Miehe, C., 2013. A phase field model of dynamic fracture: Robust field updates for the analysis of complex crack patterns. *Internat. J. Numer. Methods Engrg.* 93 (3), 276–301.
- Hoover, C., Bažant, Z., Vorel, J., Wendner, R., Hubler, M., 2013. Comprehensive concrete fracture tests: Description and results. *Eng. Fract. Mech.* 114, 92–103.
- Leon, S.E., Spring, D.W., Paulino, G.H., 2014. Reduction in mesh bias for dynamic fracture using adaptive splitting of polygonal finite elements. *Internat. J. Numer. Methods Engrg.* 100 (8), 555–576.
- May, S., Vignollet, J., De Borst, R., 2015. A numerical assessment of phase-field models for brittle and cohesive fracture:  $\Gamma$ -convergence and stress oscillations. *Eur. J. Mech. A Solids* 52, 72–84.
- Miehe, C., Welschinger, F., Hofacker, M., 2010a. A phase field model for rate-independent crack propagation: Robust algorithmic implementation based on operator splits. *Comput. Methods Appl. Mech. Engrg.* 199 (45–48), 2765–2778.
- Miehe, C., Welschinger, F., Hofacker, M., 2010b. Thermodynamically consistent phase-field models of fracture: Variational principles and multi-field FE implementations. *Internat. J. Numer. Methods Engrg.* 83 (10), 1273–1311.
- Msekh, M.A., Sargado, J.M., Jamshidian, M., Areias, P.M., Rabczuk, T., 2015. Abaqus implementation of phase-field model for brittle fracture. *Comput. Mater. Sci.* 96, 472–484.
- Needleman, A., 1987. A continuum model for void nucleation by inclusion debonding. *J. Appl. Mech.* 54 (3), 525–531.
- Needleman, A., 1990a. An analysis of decohesion along an imperfect interface. *Int. J. Fract.* 42 (1), 21–40.
- Needleman, A., 1990b. An analysis of tensile decohesion along an interface. *J. Mech. Phys. Solids* 38 (3), 289–324.
- Park, K., Paulino, G.H., 2011. Cohesive zone models: A critical review of traction-separation relationships across fracture surfaces. *Appl. Mech. Rev.* 64 (6), 060802.
- Park, K., Paulino, G., Roesler, J.R., 2009. A unified potential-based cohesive model for mixed-mode fracture. *J. Mech. Phys. Solids* 57 (6), 891–908.
- Pham, K., Amor, H., Marigo, J.J., Maurini, C., 2011. Gradient damage models and their use to approximate brittle fracture. *Int. J. Damage Mech.* 20 (4), 618–652.
- Pironi, A., Nicoletto, G., 2000. Comportamento a frattura di un adesivo strutturale. In: *Proceedings of the 15th National Congress of the Italian Group of Fracture*, IGF XV, May 3rd–5th 2000, Bari, Italy. pp. 459–466.
- Rots, J., 1988. *Computational Modeling of Concrete Fracture* (Ph.D. thesis). Technische Universiteit Delft.
- Shen, B., Paulino, G.H., 2011a. Direct extraction of cohesive fracture properties from digital image correlation: A hybrid inverse technique. *Exp. Mech.* 51 (2), 143–163.
- Shen, B., Paulino, G.H., 2011b. Identification of cohesive zone model and elastic parameters of fiber-reinforced cementitious composites using digital image correlation and a hybrid inverse technique. *Cem. Concr. Compos.* 33 (5), 572–585.
- Song, S.H., Paulino, G.H., Buttlar, W.G., 2006. A bilinear cohesive zone model tailored for fracture of asphalt concrete considering viscoelastic bulk material. *Eng. Fract. Mech.* 73 (18), 2829–2848.
- Song, S.H., Paulino, G.H., Buttlar, W.G., 2008. Influence of the cohesive zone model shape parameter on asphalt concrete fracture behavior. *AIP Conf. Proc., Am. Inst. Phys.* 973 (1), 730–735.
- Spring, D.W., Giraldo-Londoño, O., Paulino, G.H., 2016. A study on the thermodynamic consistency of the Park-Paulino-Roesler (PPR) cohesive fracture model. *Mech. Res. Commun.* 78, 100–109.
- Spring, D.W., Leon, S.E., Paulino, G.H., 2014. Unstructured polygonal meshes with adaptive refinement for the numerical simulation of dynamic cohesive fracture. *Int. J. Fract.* 189 (1), 33–57.
- Unger, J., Eckardt, S., Konke, C., 2007. Modelling of cohesive crack growth in concrete structures with the extended finite element method. *Comput. Methods Appl. Mech. Engrg.* 196, 4087–4100.

- Verhoosel, C.V., De Borst, R., 2013. A phase-field model for cohesive fracture. *Internat. J. Numer. Methods Engrg.* 96 (1), 43–62.
- Vignollet, J., May, S., De Borst, R., Verhoosel, C.V., 2014. Phase-field models for brittle and cohesive fracture. *Meccanica* 49 (11), 2587–2601.
- Volokh, K.Y., 2004. Comparison between cohesive zone models. *Commun. Numer. Methods. Eng.* 20 (11), 845–856.
- Winkler, B., 2001. Traglastuntersuchungen von unbewehrten und bewehrten Betonstrukturen auf der Grundlage eines objektiven Werkstoffgesetzes für Beton (Ph.D. thesis). Universität Innsbruck.
- Wu, J.Y., 2017. A unified phase-field theory for the mechanics of damage and quasi-brittle failure. *J. Mech. Phys. Solids* 103, 72–99.
- Wu, J.Y., 2018. A geometrically regularized gradient-damage model with energetic equivalence. *Comput. Methods Appl. Mech. Engrg.* 328, 612–637.
- Wu, J.Y., Nguyen, V.P., 2018. A length scale insensitive phase-field damage model for brittle fracture. *J. Mech. Phys. Solids* 119, 20–42.
- Wu, J., Nguyen, V., Nguyen, C., Sutula, D., Sinaie, S., Bordas, S., 2019. Chapter one - phase-field modeling of fracture. *Adv. Appl. Mech.* 53, 1–183.
- Xu, X.P., Needleman, A., 1993. Void nucleation by inclusion debonding in a crystal matrix. *Modelling Simul. Mater. Sci. Eng.* 1, 111–132.
- Zhang, P., Hu, X., Wang, X., Yao, W., 2018. An iteration scheme for phase field model for cohesive fracture and its implementation in Abaqus. *Eng. Fract. Mech.* 204, 268–287.